Brightest cluster galaxy properties and the relaxation of galaxy clusters in the IllustrisTNG simulations

Master's thesis
University of Turku
Astronomy
2025
B.Sc. Kelly Kelder
Supervisors:
Docent Pekka Heinämäki
Dr. Pasi Nurmi
Examiner:
Prof. Petri Väisänen

The originality of this thesis has been checked in accordance with the University of Turku quality assurance system using Turnitin Originality Check service.

UNIVERSITY OF TURKU
Department of Physics and Astronomy

Kelder, Kelly Brightest cluster galaxy properties and the relaxation of galaxy clusters in the IllustrisTNG simulations

Master's thesis, 61 pp.
Astronomy
May 2025

Brightest cluster galaxies (BCGs) are the predominant component of galaxy clusters which serve as important tracers for galactic and cosmic evolution. They are a powerful probe for estimating the dark matter and dark energy content of the Universe via their mass function. Insight into the dynamical state of the cluster, which is needed to investigate these relations, can be offered through the positions, kinematics, and structural characteristics of their BCGs. In this thesis, the properties of BCGs are analyzed using the TNG300-1 run of the IllustrisTNG cosmological hydrodynamical simulation project. The study focuses on the relation of BCGs to its host cluster mass, dynamics, and substructuring. A variety of observationally motivated indicators, such as the magnitude gap, peculiar velocities, and BCG central offsets, are used to explore the relaxation of these galaxy clusters.

The analysis confirmed that BCG mass and half-mass radius strongly correlate with the corresponding properties of its host cluster, implying that the BCG growth rate is directly related to the growth of the cluster. Dynamical analysis revealed that the majority of BCGs reside near the cluster potential well, with over 95% of them having an offset smaller than their half-mass radius. Comparisons across redshift demonstrate a clear trend toward increased BCG centrality and dynamical relaxation over time. As a comparison, clusters with greater BCG offsets in the current epoch show to have a narrow magnitude gap, indicating dynamical disturbances and possible substructuring within them. The analysis of cluster substructures, done via Gaussian mixture modeling, showed that most commonly (in $\sim 30\%$ of the cases) these systems exhibited two substructures, implying again that the entire set of clusters cannot be assumed to be dynamically relaxed. When applying the virial theorem and center of mass shift criteria, around 20% of clusters at $z = 0$ are considered to be in dynamical equilibrium, reinforcing the need for careful consideration of dynamical state in both simulation and observational studies. These findings contribute to a broader understanding of BCG formation and evolution and offer proxies for evaluating cluster relaxation in future observational work.

Keywords: brightest cluster galaxies, cluster dynamics, hydrodynamical simulations

Contents

Acknowledgments

First and foremost, I'd like to thank my supervisors Pekka Heinämäki and Pasi Nurmi for guiding me through the data exploration and giving interesting ideas for the analysis part of the thesis work. I am especially grateful for Pekka's readiness in providing me immediate feedback on my progress. Additionally, I want to thank my coursemates Anastasiia and Evangelos for supporting me through every step of my MSc studies and I really appreciate us helping each other out during challenging coursework assignments. I feel very fortunate to have such warm and supportive friends surround me, both here in Turku and back in Tartu – all of them have made the past two years especially exciting and memorable. Lastly, I am truly thankful to my parents for giving me the opportunity to come study in Finland through both financial and moral support.

Introduction

Brightest cluster galaxies play a crucial role in cosmic structure formation, serving as key tracers of galaxy evolution across different mass scales. Their superior luminosity enables high-redshift observations, providing insight into their formation and evolution. According to The Central Galaxy Paradigm (van den Bosch et al., 2005), the systems are typically assumed to have formed early on through hierarchical structure formation and to have reached dynamical equilibrium in the cluster center. The assumption of the systems being relaxed is fundamental in many conclusions about their properties and their application in cosmology. Most notably, it is used to determine cluster masses and, by that, via the mass function, to estimate values for cosmological parameters related to the dark matter and dark energy content in the Universe (Voit, 2005).

Yet, galaxy clusters are not a homogeneous ensemble of systems; their masses, dynamical properties, and evolutionary stages vary greatly, and therefore the conditions needed for relaxation are not always achieved or may have been temporarily lost. In observational studies, this is expressed in peculiarities such as unexpected brightest galaxy central offsets, high peculiar velocities, and alignment of the BCG with respect to the orientation of the cluster (e.g. Lopes et al., 2018; De Propris et al., 2020). Thus, there is strong theoretical and observational interest in understanding and identifying brightest galaxy and host system property-related indicators that signify the relaxation of the host system and contribute to their formation. In addition to the local environment, the properties and evolution of brightest cluster galaxies are reported to be influenced by the surrounding cosmic web, their location in the large-scale density field, and connections to galaxy filaments (e.g. West et al., 2017; Einasto et al., 2024). Due to the complexity of this issue, the theoretical basis of these interactions is still poorly understood.

Solving this matter has only become recently possible through state-of-the-art

hydrodynamical simulations, such as IllustrisTNG. The large-scale simulations provide a laboratory for analyzing these discrepancies in great detail. In this work, I examine the galaxy clusters in the TNG300-1 simulation box to study the properties of their brightest galaxies, compare the findings to currently existing observational results, as well as discuss reasons for possible differences and considerations needed to take into account to assess the results correctly.

The structure of the thesis is the following. In Chapter 1 the cosmological background and structure formation will be explained along with details concerning the formation of clusters and their brightest galaxies. Chapter 2 covers the details about cosmological simulations and how hydrodynamical simulations, including IllustrisTNG, are run. After this, Chapter 3 goes into further detail about the brightest cluster galaxy properties, things we know from currently published studies, and properties that are going to be analyzed in this work. In Chapter 4, everything regarding the selection of data, its analysis and the results of the properties of the clusters and their brightest galaxies (including their dynamical properties, substructures, evolution and dynamical state) will be discussed. Finally, in Chapter 5 the main results are summarized and the final conclusions are made.

1 Cosmological background

1.1 The cosmological model

Cosmology considers the Universe as a whole. It studies its structure and evolution to answer questions regarding how the structures we currently see have formed and predict what will be the future. The history of the Universe has been extensively researched creating theoretical frameworks and models. The current leading theories for structure formation are based on the Λ Cold Dark Matter (ΛCDM) cosmology with the assumption that the Universe is homogeneous and isotropic at large scales – i.e. the galaxy distribution is independent of position and direction. The model is well supported by statistical analysis and observations. With further data from WMAP (Wilkinson Microwave Anisotropy Probe) and Planck, the parameters of this paradigm have been well constrained. The values obtained showed excellent consistency with independent measurements; the baryon density aligned with estimates from cosmic nucleosynthesis, the Hubble constant was in accordance with values determined through direct measurements, and the implied large-scale clustering in today's Universe matched the findings from extensive galaxy surveys and weak gravitational lensing studies (Mo et al., 2010, and references therein).

In the ΛCDM model, the Universe is flat and dominated by non-relativistic (i.e. cold) dark matter particles. Under these assumptions, the metric in the Einstein field equation, which determines the geometry of the four-dimensional spacetime, can be expressed as the Robertson-Walker metric

$$ds^2 = c^2dt^2 - a^2(t)\ \left[\frac{dr^2}{(1-kr^2)} + r^2(d\theta^2 + \sin^2\theta\ d\phi^2)\right], \tag{1}$$

where $(r,\ \theta,\ \phi)$ are co-moving spherical coordinates, c is the speed of light and $a(t)$ is the scale factor. The constant k represents the curvature of space, where $-1,\ 0,\ 1$ account for an open saddle-like, flat and closed spherical Universe accordingly. With the ratio of the scale factor to its time derivative, we can define the Hubble parameter

to describe the expansion of the Universe

$$H(t) = \frac{\dot{a}(t)}{a(t)}. \tag{2}$$

By approximating the matter and energy content in the Universe as an ideal fluid, the Einstein field equation can be solved with the Robertson-Walker metric, yielding the Friedmann-Lemaître equations:

$$\frac{\ddot{a}}{a} = -\frac{4\pi G}{3}\left(\rho + \frac{3P}{c^2}\right) + \frac{\Lambda c^2}{3}, \tag{3}$$

$$\frac{\ddot{a}}{a} + 2\left(\frac{\dot{a}}{a}\right)^2 + \frac{2kc^2}{a^2} = 4\pi G\left(\rho + \frac{P}{c^2}\right) + \Lambda c^2, \tag{4}$$

where the two can be combined to obtain

$$\left(\frac{\dot{a}}{a}\right)^2 = \frac{8\pi G}{3}\rho - \frac{kc^2}{a^2} + \frac{\Lambda c^2}{3}, \tag{5}$$

here P is the total pressure and ρ the total density of the Universe, G is the Newtonian gravitational constant and Λ the cosmological constant corresponding to dark energy and accounting for the main factor in driving the expansion of the Universe. If $k = \Lambda = 0$, the density ρ reaches a critical value

$$\rho_c = \frac{3H^2}{8\pi G}. \tag{6}$$

The critical density is used to define a dimensionless density parameter

$$\Omega_0 = \frac{\rho_0}{\rho_c}, \tag{7}$$

which is defined for each matter–energy component of the Universe: matter (baryonic and dark matter) Ω_m, dark energy Ω_Λ and radiation Ω_r. These are used to characterize cosmological models, where their sum, the total density parameter $\Omega = \Omega_m + \Omega_\Lambda + \Omega_r$, determines the geometry of the Universe. If $\Omega < 1$, the Universe is negatively curved (open), if $\Omega = 1$, the Universe is flat, and if $\Omega > 1$, the Universe is positively curved (closed) (Mo et al., 2010).

1.2 Hierarchical structure formation

The large-scale structure of the Universe, as we know it, is believed to have formed from small density perturbations caused by quantum fluctuations in the early Universe. A common understanding of this is that during the linear regime, small regions which had a slightly higher density compared to the mean would attract their surroundings more, causing matter to concentrate and making the regions strongly over-dense. In contrast, matter from the under-dense regions would flow away due to the gravitational influence being weaker, making the regions even more scarce of material. With expansion, the so-called emptier regions would become extensive voids, whilst gas in the denser regions would later via cooling form filaments composed of galaxies and galaxy clusters within large dark matter halos.

In a more quantitative sense, the evolution of density fluctuations can be described by the Linear Perturbation theory approximation with a second-order differential equation, derived from the continuity, Euler, and Poisson equations as

$$\ddot{\delta} + 2H\dot{\delta} - 4\pi G\bar{\rho}\delta = 0, \tag{8}$$

where $\delta = d\rho/\bar{\rho}$ is the density contrast parameter and $\bar{\rho}$ the mean matter density. The equation has a growing mode solution in the form

$$\delta(\mathbf{x}, t) = D(t)\ \tilde{\delta}(\mathbf{x}), \tag{9}$$

i.e., the spatial and temporal dependencies factorize. Here $\tilde{\delta}(\mathbf{x})$ is an arbitrary function and the growth factor $D(t)$ satisfies the condition

$$\ddot{D} + 2H\dot{D} - 4\pi G\bar{\rho}(t)\ D = 0. \tag{10}$$

In a special case of the Einstein-de Sitter model ($\Omega_m = 1,\ \Omega_\Lambda = 0$), the solution reaches a form where the growth factor is equal to the scale factor $a(t)$, and therefore in the matter-dominated era, the density perturbations are linear:

$$\delta \propto a(t) \ll 1. \tag{11}$$

At around $z \sim 30 - 50$, the cooling becomes sufficient to commence the formation of stars and galaxies. At this stage, the density contrast factor starts reaching the value 1, after which the perturbations become nonlinear (Mo et al., 2010).

Since dark matter interacts mainly gravitationally, its density perturbations began to grow earlier, meaning that the baryonic structures were growing within already existing gravitational dark matter wells (Schneider, 2006; Mo et al., 2010). According to the standard theory of galaxy formation, the cooling of hot gas inside the already virialized dark matter halos leads to matter accumulation at the center of the halo's gravitational potential well. This is especially evident in the case where the cooling time is shorter than the dynamical time, as the matter cannot reach hydrostatic equilibrium but rather accretes directly onto the central protogalaxy. In case of slower cooling, the same effect can be discerned, because even in case of reaching equilibrium, the denser inner regions may lose pressure support and flow onto the central object. This means that in any case cooling causes baryonic matter to segregate from dark matter and accumulate to the center as dense, cold gas, leading to the formation of a galaxy at the center of the dark matter halo.

The hierarchical structure formation depicts a "bottom-up" formation scenario in which these dark matter halos merge to form even larger structures. The smaller halo becomes a subhalo, and its central galaxy becomes a satellite galaxy, where it no longer accretes hot gas – all the gas will accumulate in the center of the potential well (Kauffmann et al., 1993; Somerville & Primack, 1999; Cole et al., 2002). Due to accretion, the new central galaxy begins to grow, leading to the deduction that it should become the most massive and brightest within the halo. This idea is supported by the fact that, in case of the existence of another large galaxy, due to dynamical friction, it is expected to eventually sink into the potential minimum and merge with the first galaxy, hence leading to the formation of an even larger central galaxy. The paradigm, named the Central Galaxy Paradigm, therefore strongly

indicates that the brightest galaxy will always reside at the center of the cluster's dark matter halo. This approach, of course, is a very simplified version, as the final outcome depends heavily on other interactions taking place within the halo. The Central Galaxy Paradigm is considered a statistical statement and may not hold in each individual case, e.g. in non-virialized or strongly interacting systems (van den Bosch et al., 2005).

1.3 Formation of galaxy clusters

Clusters form as a direct result of hierarchical structure formation. As dark matter halos merge, the structure becomes progressively more complex. First, in case of single galaxy halo mergers, the two galaxies start orbiting around the potential well of a common dark matter halo. Due to tidal stripping and dynamical friction, material is removed from the galaxies and the orbital energy of the components is decreased, leading the orbits to decay over time. The orbit decay time can depend on various factors, such as the mass ratio of the merging halos, eccentricity of their orbits, and mass loss from tidal stripping. The components may not merge, but remain in a system where the larger of the galaxies makes its way to the gravitational potential well of the halo, while the other remains a smaller satellite galaxy. As discussed in the previous section, further mass accretion will be done mainly by the central component. Dark matter halos containing multiple member galaxies can in turn merge, leading to the formation of groups and clusters of galaxies (Kauffmann et al., 1993). Factors such as the gravitational effects of dark matter, large decay timescales, disruptions caused by galaxy interactions, AGN feedback, and constant ongoing star formation due to the feeding of the clusters via filaments lead to the systems not merging to a single galaxy, but to a gravitationally preferred cluster system (Mo et al., 2010). It is important to note that the cooling remains effective up to masses of around $10^{12} - 10^{13}$ $M_{\odot}$. Beyond this point, the increasing gas density

and temperature prevent the cooling time from becoming shorter than the dynamical time; as a result, the structure is unable to collapse into a single extremely massive galaxy (e.g., Binney, 1977; Silk, 1977; Rees & Ostriker, 1977). Galaxy clusters are described as the most massive gravitationally bound and relaxed cosmic structures. Relaxation means that the system is in dynamical equilibrium (forces are balanced), virialized (follows the virial theorem) and has a smooth morphology (no strong signs of substructuring). However, it is important to note that due to mergers and the accretion of material from filaments, clusters can often be out of equilibrium for a certain time during their evolution (Neto et al., 2007; Mo et al., 2010).

A significant fraction of galaxies in the present-day Universe are located in groups ($\sim 48\%$, Tempel et al., 2014) and clusters ($< 10\%$) in which the number density of galaxies is a few tens to a few hundred times higher than the average. As defined by Mo et al. (2010), the densest, most populous, and most massive virialized systems are called galaxy clusters, which typically contain more than 50 relatively bright galaxies in a volume only a few megaparsecs across. There, however, is no actual well-defined boundary between groups and clusters since they form a continuum on systems with widely ranging masses. George Abell first classified clusters as systems with at least 50 members with apparent magnitudes $m < m_3 + 2$, but also listed poorer clusters with richness between 30 and 50 members (Mo et al., 2010). Since the richness limit is not a strict physical threshold, it varies across different studies depending on the specific requirements of the work. For instance, De Propris et al. (2020) follow the same richness limit of $\lambda > 50$, Seppi et al. (2023) restrict the richness by $\lambda > 20$, whereas, similarly to Chu et al. (2021), some studies may not even limit the clusters based on the number of galaxies they host.

Due to their large masses, clusters are an important tool in cosmology as they can be used as probes to provide cosmological constraints, complementary to those based on analysis of the CMB, stellar clusters, supernova luminosity distances, and

gravitational lensing (Ludlow et al., 2012; Planck Collaboration et al., 2020). Their cosmological evolution is linked to the growth of cosmic structures. Due to their high galaxy density, groups and clusters provide an ideal setting for investigating galaxy interactions and their influence on the overall galaxy population. For instance, the prevalence of elliptical galaxies in clusters suggests that local galaxy density plays a significant role in shaping their morphology and evolution (the so-called morphology-density relation, Dressler et al., 1997; Schneider, 2006).

2 Cosmological simulations

Interpreting the results of observational data requires a good understanding of the theoretical basis of the properties and evolution of galaxies. Once the density perturbations become non-linear ($\delta \geq 1$), using cosmological simulations is essentially the only way to deal with this complex issue. The main building blocks for these models consist of dark matter, which is responsible for the structure formation, and dark energy that is accountable for the accelerated expansion of the Universe. Despite us not knowing about the nature of these two, simulations are able to make reliable predictions just based on some general characteristics using N-body simulations. Even though visible matter, i.e. baryons, comprises only about five percent of the energy of the Universe, it is essential to incorporate them into simulations to be able to study galaxies (Vogelsberger et al., 2019). However, introducing baryonic processes is a challenging aspect that adds a strong computational strain on the simulation. Over the last years simulations have evolved to an extent where large-scale simulations incorporating both dark matter and baryons are possible to run at large scales.

2.1 Hydrodynamical simulations

Hydrodynamical simulations combine dark matter N-body simulations with baryons. The interactions between the two affect the composition of dark matter on smaller scales which is especially important to consider when looking at the internal structure of dark matter halos (Vogelsberger et al., 2019).

The simulations are given initial conditions, which specify the perturbations imposed on top of a homogeneous expanding background – typically a spatially flat Friedmann-Lemaître-Robertson-Walker spacetime with defined composition of dark matter, dark energy and baryons. This is in accordance with the ΛCDM model. The simulation particles are placed in a uniform Cartesian lattice or glass-like parti-

cle configuration using a linear theory approximation (see Chapter 1.2) or low-order perturbation theory. Based on the Zeldovich approximation, the matter power spectrum (MPS) is applied to the lattice to configure a disturbed field which follows the MPS distribution. A gravitational "glass" is composed by moving particles from random initial positions using the opposite sign of gravity until they freeze in comoving coordinates. The positions and velocities of baryons are set in a similar way, and their temperature is often roughly initialized to the CMB temperature. The baryon component starts off as gas, mostly hydrogen and helium. The gas component is typically described as an inviscid ideal gas following the Euler equations. During the structure formation step, part of the cold and dense gas will eventually be turned into collisionless star particles. The distribution and evolution of dark matter are described by the collisionless Boltzmann equation paired with the Poisson equation, which outlines the gravitational potential. A more detailed description of the evolution of each component is provided by Vogelsberger et al. (2019).

Other aspects that need to be taken into account when creating a cosmological simulation entail the choice of the simulation volume and resolution. As even state-of-the-art simulations cannot capture all relevant scales, hydrodynamic simulations are typically separated into two categories: uniformly sampled periodic large-volume simulations and zoom simulations, where the specific area of focus is highly resolved and depends strongly on the mass of the studied object. For the sake of this research, we will focus more specifically on large-volume simulations. Large-volume simulations, such as EAGLE (Schaye et al., 2015), Magneticum (Biffi et al., 2013), Illustris (Nelson et al., 2015), and the latest IllustrisTNG (Nelson et al., 2018, used in this work), apply periodic boundaries to mimic the large-scale homogeneity and isotropy of matter distribution in the Universe.

2.2 IllustrisTNG simulation

The simulations known as IllustrisTNG are large-scale cosmological models conducted with the AREPO moving-mesh code. AREPO (Springel, 2010) models cosmic gas dynamics using a mesh based on Voronoi tessellation. It is generated from a set of control points that can move with the velocity of the local flow, allowing to obtain a Lagrangian formulation of continuum hydrodynamics that does not suffer from the mesh distortion limitations intrinsic to other mesh-based Lagrangian schemes (see Springel, 2010; Nelson et al., 2018, for more details).

These simulations incorporate gravo-magnetohydrodynamics and are organized into three distinct volumes: TNG50, TNG100, and TNG300 with three different runs with varying resolution in each volume. All TNG runs start from cosmologically motivated initial conditions, assuming an updated cosmology consistent with the Planck Collaboration et al. (2016) results (shown in Table I) with Newtonian self-gravity solved in an expanding Universe.

Table I. Cosmological parameters used in the TNG simulation suite. From left to right: dark energy density parameter, matter density parameter, baryon density parameter, amplitude of the matter power spectrum, scalar spectral index and dimensionless Hubble parameter.

$\Omega_{\Lambda,0}$	$\Omega_{m,0}$	$\Omega_{b,0}$	σ_8	n_s	h
0.6911	0.3089	0.0486	0.8159	0.9667	0.6774

Each run solves for the coupled evolution of dark matter, luminous stars, cosmic gas and supermassive black holes from a starting redshift of $z = 127$ to the present epoch, $z = 0$. In the current work, I will focus on the TNG300-1 run specifically as it is the largest simulation box with the highest resolution at these large scales, allowing to analyze galaxy clusters with the best accuracy. The main properties and parameters of this run, such as size, resolution, and particle masses, are shown in Table II. Since the spatial resolution of hydrodynamical simulations is highly adaptive, it can not

Table II. Some physical and numerical parameters for the TNG300-1 run. From left to right: the box volume, box side length, initial number of gas cells and dark matter particles, the target baryon mass, dark matter particle mass, minimal physical gas cell radius measured at $z = 0$, the median gas cell radius ($z = 0$). For more details regarding the parameters, refer to Nelson et al. (2018)

Volume [cMpc^3]	$L_{\rm box}$ [cMpc/h]	$N_{\rm GAS,\ DM}$ –	$m_{\rm baryon}$ [M$_\odot/h$]	$m_{\rm DM}$ [M$_\odot/h$]	$r_{\rm cell,\ min}$ [pc]	$\bar{r}_{\rm cell}$ [kpc]
302.6^3	205	2500^3	$7.6 \cdot 10^6$	$4.0 \cdot 10^7$	47	31.2

be described by a single number but rather a distribution. Figure 1 shows the distribution of Voronoi gas cell sizes in the three simulations, where TNG300 is marked in orange. The figure highlights the high spatial resolution in star-forming gas (i.e., within galaxies); whereas the largest gas cells are located in the low-density intergalactic medium. To evolve these high-resolution runs to redshift zero, an order of 10 million individual time steps are needed. The group and subgroup catalogs are computed during the simulation using the Friends-of-Friends (FoF) and SUBFIND substructure identification algorithms.

2.2.1 Friends-of-Friends (FoF)

The FoF algorithm has been historically used to define groups and clusters of galaxies in observations, and has also been adopted to identify them within simulations (Davis et al., 1985). The algorithm considers two particles to be members of the same halo (that is, "friends") if their separation is smaller than a given linking length, typically $b = 0.2$, which corresponds to 180 times the average global density. This value refers to the theoretical virialization criterion of the dark matter halo in the spherical collapse model. The linking length is the only free parameter of the method, defined as the mean interparticle separation (Kravtsov & Borgani, 2012). The algorithm iterates over all particles, first identifying neighbors within the linking

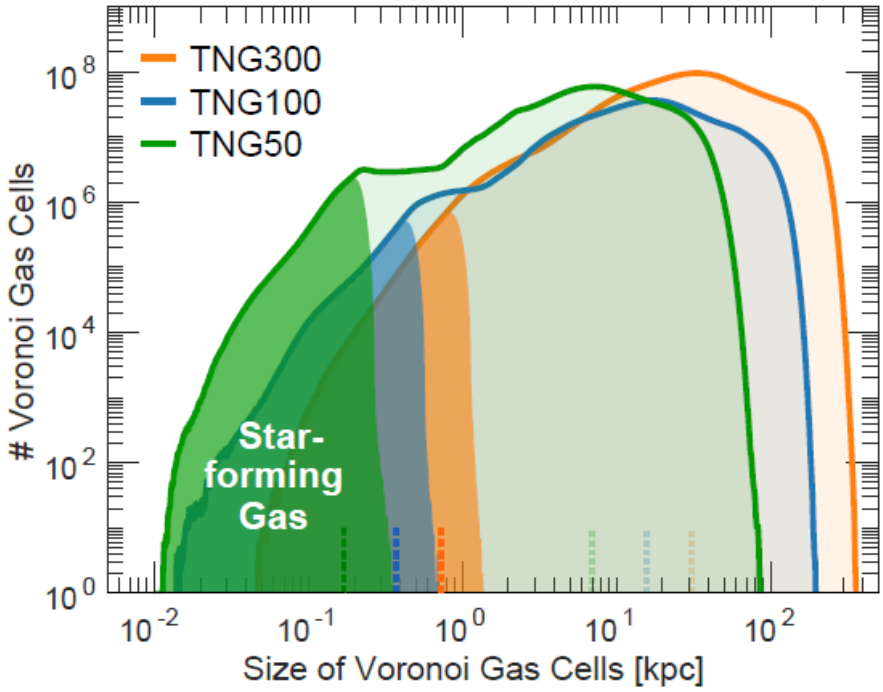

Figure 1. The spatial resolution of the TNG simulations at $z \sim 0$. The highlighted regions of the distributions refer to star-forming gas inside galaxies. The median values are indicated by vertical dotted lines (Nelson et al., 2018).

length for each particle i, then extending the group by evaluating the neighbors of these neighbors. Any particle within a distance less than b from any group member is included. This process continues until no further particles meet the criterion, finalizing the group structure. With the given linking length, this algorithm is unable to detect substructures within larger virialized objects; therefore, a different algorithm, SUBFIND, is used to tackle the issue of substructure identification.

2.2.2 SUBFIND

The SUBFIND algorithm (Springel et al., 2001) is created to extract locally over-dense self-bound particle groups within a larger parent group (in practice, galaxies within a cluster). For the purpose of this simulation, the authors use the FoF groups as input data for the SUBFIND algorithm. The algorithm starts by computing a local density estimate at the positions of all particles in the input group. All locally

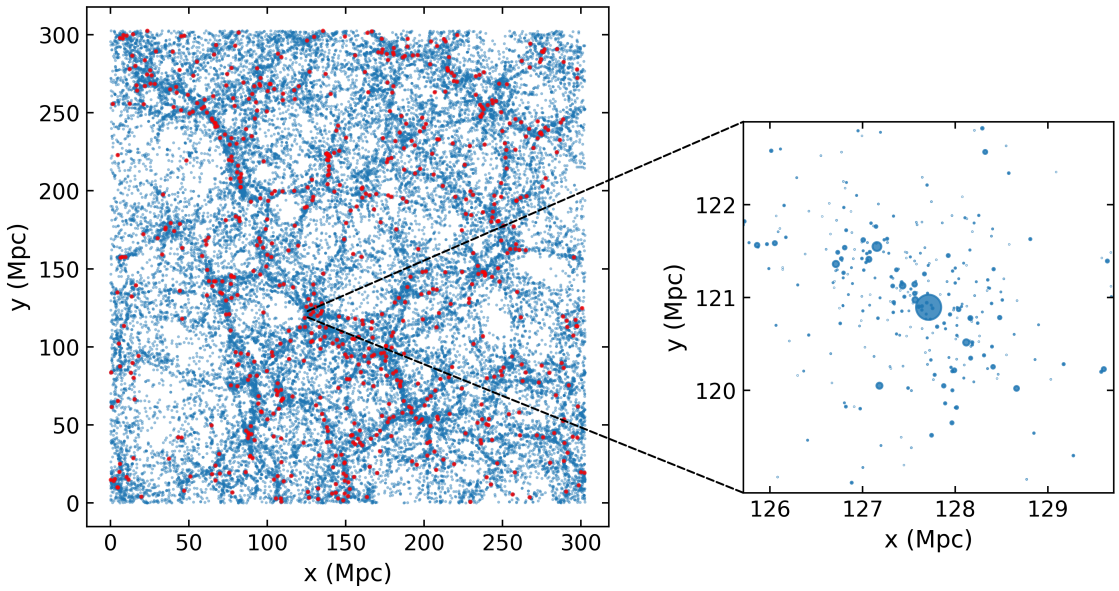

Figure 2. Galaxies (blue) and cluster centers (red) in the slice of the TNG300-1 simulation box at $z \in [30, 90]$ Mpc. The zoom panel shows an example of a galaxy cluster with 362 members. The size is scaled by the galaxy stellar masses.

overdense regions (simulation particles) are identified by progressively lowering the density threshold, and any region that has a density greater than the local average is considered a substructure candidate. The densities of these candidates are compared with those of their neighbors. The subgroups are grown around the particles with the highest density until all of the particles are assigned to a subgroup.

Next in the algorithm, the boundedness of the particles assigned to the subgroups is checked. Each subhalo candidate is subjected to an unbinding procedure in which particles with positive total energy are removed, until only bound particles remain. This ensures that the remaining substructures are part of a self-bound particle group. The unbinding takes into account the subhalo's center as the coordinates of the most bound particle, and the velocity center is taken as the mean velocity of all particles in that group. Physical velocities relative to the group center are obtained by adding the Hubble flow to each particle's peculiar velocity. If more than a threshold value of particles remains, they form a subhalo. To make sure that each particle is assigned to a subhalo only once, the final assigning is done in an inverse sequence as they

have been generated in, i.e. the subgroup particles are worked through from low to high density to ensure that a smaller subhalo within a larger subhalo will always be processed later than its parent subhalo, and the label assigned to it will belong to the latest classification. An example of the layout of the halos (clusters) and subhalos (galaxies) in the TNG300-1 simulation box is shown in Figure 2.

3 Brightest cluster galaxies

Out of all cluster members, the brightest galaxies hold a particularly significant status – being expected to reside close to the potential well of their host cluster, their properties and evolution are closely linked to those of their host environment (Marini et al., 2021). As a result of the dynamical friction that takes place during hierarchical structure formation in the center of newly formed large dark matter halos, the material accreted by the central galaxy causes it to grow rapidly. Due to this rapid accretion, BCGs are typically observed as early-type elliptical galaxies that show little evidence of ongoing star formation, despite their large masses (Kravtsov & Borgani, 2012). The formation and growth are commonly described by a two-phase formation model: an initial ($z \geq 2$) in situ star formation driven by infalling cold gas in the central galaxy, followed by an extended phase (around $z \leq 3$) during which ex situ stars are primarily accreted to the central galaxy (Oser et al., 2010). These mergers play a crucial role in comprising the brightest galaxies, as it has been noted that the majority of the final mass is bound to these galaxies at late evolutionary stages (i.e., half of the final mass is reached at $z \sim 0.5$, De Lucia & Blaizot, 2007). At the same time, various quenching mechanisms, such as AGN feedback and shock heating, act to suppress further star formation, especially in the dense cores of massive halos, contributing to the passive nature of these brightest galaxies (Croton et al., 2006).

Although these systems have been dubbed the brightest cluster galaxies, the exact definition of a BCG often depends on the focus of a given study, making it essential to clarify the selection criteria before drawing comparisons between different studies. In many cases, the BCG is simply identified as the most luminous galaxy within the cluster (e.g. Cui et al., 2016; Dalal et al., 2021). However, additional factors are sometimes considered, such as morphology – for instance, Lauer et al. (2014) include only elliptical galaxies — or, in observational studies, the spatial extent of

the cluster is often also taken into account (e.g. Lopes et al., 2018; De Propris et al., 2020; Chu et al., 2022). Alternatively, the BCG can be defined as the most massive galaxy or the one residing in the center of the host cluster's potential well, as was done by Pillepich et al. (2018). In this work, I adopt a straightforward approach, defining the BCG strictly as the galaxy with the highest luminosity.

As suggested by the paradigm, these brightest galaxies are often located near the clusters' potential minima. However, since the location of the gravitational potential well is not observable, a proxy often used for observations is the location of the X-ray luminosity peak. The offset between the location of the BCG and the peak of the X-ray emission by the hot gas in the cluster has been observed to be typically small. For instance, Haarsma et al. (2010) found that around 90% of clusters at $z < 0.2$ host a BCG within 30 kpc of the X-ray peak, and a study by Rossetti et al. (2016) obtained a median BCG offset of 21.5 kpc. Furthermore, BCGs are assumed to move in unison with their host cluster, that is, their observed peculiar velocities are expected to be low (e.g. Lauer et al., 2014). As a key tracer for its host cluster properties, the BCG dynamical and structural properties can be investigated to draw conclusions on the cluster state and evolution. Due to the close link between the cluster and its brightest galaxy, BCGs can be directly used to probe cosmological constraints under the preliminary assumption that the systems are dynamically relaxed. The dynamical state of the cluster plays an important role in these conclusions, as in case the system is not relaxed, the mass profiles, and therefore the cosmological constraints, will be evaluated incorrectly (e.g. Kravtsov & Borgani, 2012; Lauer et al., 2014). In particular, this is due to the fact that out-of-equilibrium systems lead to underestimating the cluster virial masses, and therefore the cluster mass function, which directly influences the inferred values of parameters Λ, Ω_m, and σ_8, relating to the assumptions of structure formation and the expansion of the Universe (Voit, 2005; Allen et al., 2011).

To assess cluster relaxation, studies such as Zhang et al. (2022) and the references therein suggest using observable properties that are generally associated with relaxed and unrelaxed clusters. For instance, dynamically relaxed clusters are typically expected to exhibit a nearly spherical morphology and a line-of-sight velocity distribution that follows a Gaussian profile (Faltenbacher & Diemand, 2006). In contrast, unrelaxed clusters often show significant deviations from this velocity distribution (e.g. Hou et al., 2009) and are characterized by the presence of massive substructures, as well as a small magnitude gap between the two brightest member galaxies (Lopes et al., 2018). Given the strong connection between the BCG and its host cluster properties, it is reasonable to expect that the observable properties of the BCGs can also provide estimates of cluster relaxation.

In this work, I analyze the dynamical state of galaxy clusters (defining them as either dynamically relaxed or not relaxed) through their brightest galaxy properties. I use characteristics such as BCG central offsets, peculiar velocities, the magnitude gap between the two brightest members, and the number of substructures present in each cluster to assess this matter and provide indicators for cluster relaxation through directly observable traits.

4 Analysis and results

This chapter outlines the key characteristics of the analyzed systems. Firstly, Section 4.1 introduces the selection criteria for the clusters and galaxies. Section 4.2 examines the general properties of BCGs and their relation to the host systems. In Section 4.3, the dynamical properties of the BCGs, such as the central offsets and peculiar velocities, will be covered. Section 4.4 focuses on the cluster evolution, namely, to investigate how certain BCG and cluster properties evolve from redshift $z = 1$ to the current epoch. Substructuring within the clusters will also be explored in this section. Lastly, Section 4.5 assesses the dynamical state of the clusters and determines observational indicators for cluster relaxation.

4.1 The data

The main data set was acquired from the IllustrisTNG website[1] as a $z = 0$ group catalog and downloaded and run locally. The information in the files was imported using a Python code provided in the IllustrisTNG tutorial. In addition, data at $z = 0.33,\ 0.68,\ 1$ were used to get an overview of the properties of cluster evolution.

Since the focus of the work was on galaxies and clusters of galaxies, certain filtering steps were necessary to obtain meaningful data. The data reduction for subhalos was done following Galárraga-Espinosa et al. (2020). Firstly, all objects in the catalog flagged with a false SubhaloFlag variable were removed – these are objects that the SUBFIND algorithm has deemed as subhalos but they have not followed the usual processes of galaxy formation, instead they have originated from other types of baryonic processes. For the remainder, a lower limit was applied for the stellar mass of the subhalos. Based on observational studies (e.g., Brinchmann et al., 2004; Taylor et al., 2011), a subhalo can be considered a galaxy when its stellar mass is at least of 10^9 $M_\odot$. No upper mass limit was provided to ensure that

[1] https://www.tng-project.org

no BCGs would be removed from the sample. The most massive object in the set had a stellar mass of $7.8 \cdot 10^{12}$ $M_\odot$. Regarding halos, the lower limit for the virial mass was chosen as $M_{200} > 10^{13}$ $M_\odot$ to ensure that the halos are large enough to surround clusters of galaxies. In addition, the sample was limited to clusters with at least 20 galaxies. This selection was done to provide enough data for a reliable statistical analysis.

Due to periodic boundary conditions, it was also vital to filter out halos that are located on the edges of the simulation box, as they might be divided into two along the simulation box edge. For this, a limit that the halo center must be at least 2 Mpc from the simulation box edge was chosen. At $z = 0$, the final sample contained 945 clusters and 45614 galaxies therein.

4.2 BCG properties

The brightest galaxy in each cluster was defined based on the r-band magnitude. The absolute r-band magnitudes of the BCGs are compared with those of the other galaxies in the dataset in Figure 3. The same definition was used to determine the second brightest cluster galaxies (SBCGs, also shown in the figure). As expected, the BCG r-band magnitude distribution has notably smaller values compared to the other cluster members; however, there are also systems in which the magnitudes of the two brightest members are quite similar. An example of one of these TNG cluster systems is provided in Figure 4. This cluster has 329 member galaxies with the BCG and SBCG shown in different colors. The sizes of the points represent the stellar masses of each galaxy; hence the BCG and SBCG are of similar size due to the stellar mass and magnitude correlation. The locations of the cluster potential well and center of mass are marked with crosses and the black circle demonstrates the area within the virial radius (R_{200}) of the cluster. In the case of this cluster, it can be observed that the SBCG is located outside of the virial radius and seems

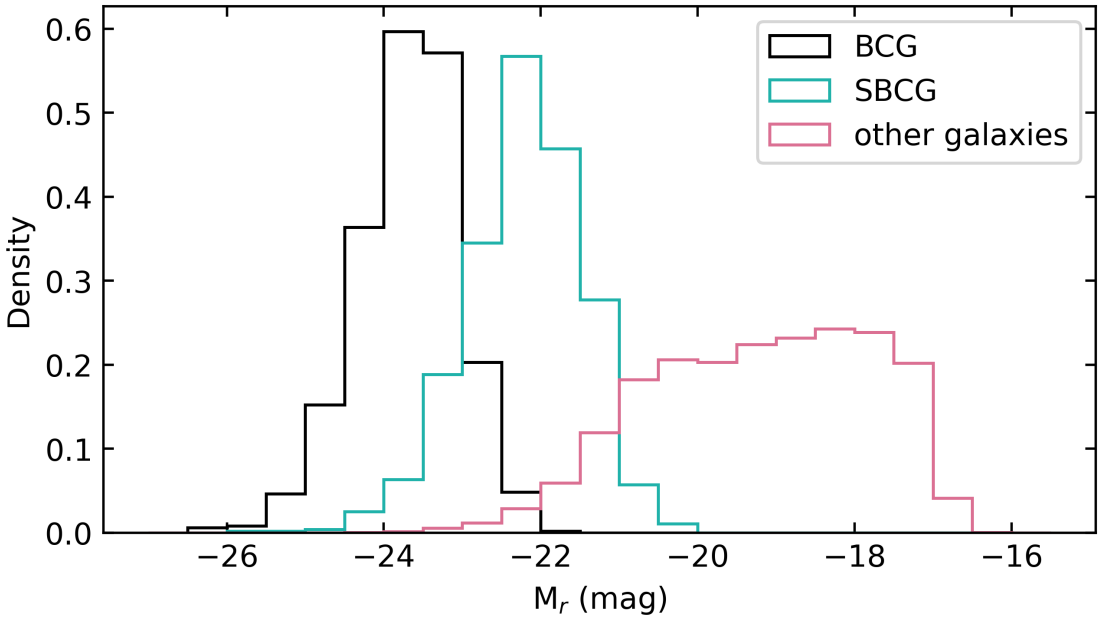

Figure 3. Absolute r-band magnitude distribution of the brightest, second brightest and the remaining galaxies within the clusters. The median values for the distributions are −23.6, −22.2 and −19.1 mag respectively.

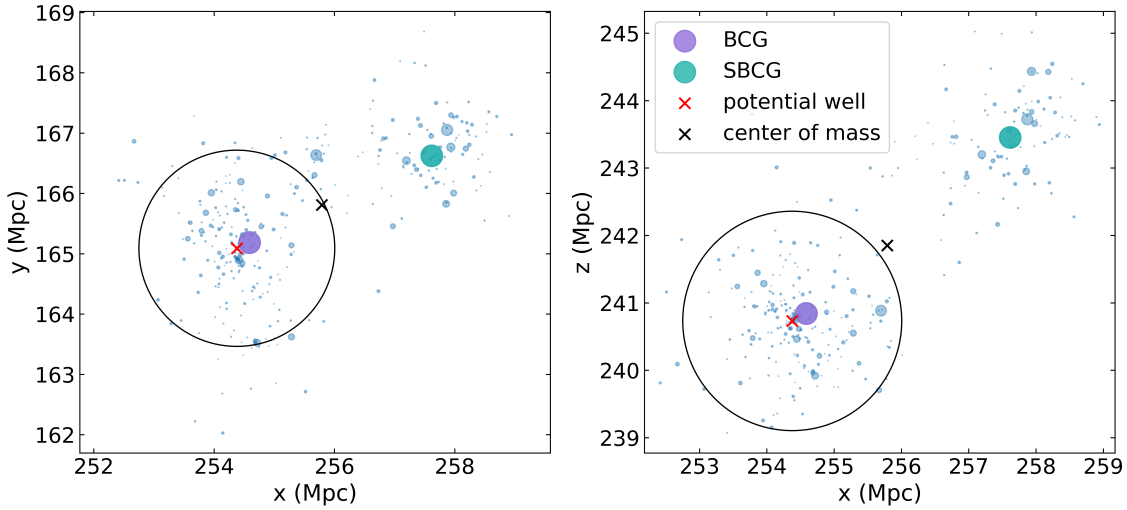

Figure 4. An example of a plane projection of a cluster with 329 members. The member galaxies are marked with blue dots where the marker size represents the galaxy stellar mass. The BCG and SBCG are shown in separate colors. Crosses indicate the locations of the cluster center of mass and potential well and the area within the virial radius is surrounded by a black circle.

to be forming a separate substructure within the cluster. Details concerning these properties will be discussed in the upcoming chapters.

4.2.1 Mass relations

The BCG and SBCG stellar masses were analyzed as a function of the host cluster's virial mass. The relations are visible in Figure 5 and it can be seen that for BCGs, there is a strong correlation between these values, which indicates that larger clusters are also capable of hosting more massive galaxies. This dependency is also visible for SBCGs, but in this case there is a stronger dispersion along the y-axis. For all other cluster members (not shown in the figure), the stellar mass dispersion is even more prominent, meaning that the BCGs have a unique relation to the halo masses. This relation, in units of solar masses, can be expressed as:

$$\log \mathrm{M}_* = (0.795 \pm 0.012) \log \mathrm{M}_{200} + (0.749 \pm 0.165) \tag{12}$$

which is also shown in the figure as the black dashed line. The errors shown here (and in future plots) are the standard errors given by the linear regression model. Previously done observational studies also show a correlation between the BCG stellar mass and cluster virial mass. For instance, Erfanianfar et al. (2019) find the relation to be $\log \mathrm{M}_* = (0.41 \pm 0.04) \log \mathrm{M}_{200} + (5.59 \pm 0.54)$ (red line in Figure 5), which is a slightly weaker correlation than for the current simulated data. Similarly, Kravtsov et al. (2018) found a relation of $\log \mathrm{M}_* = (0.39 \pm 0.17) \log \mathrm{M}_{500} + (12.15 \pm 0.08)$ and Oliva-Altamirano et al. (2014) show a power-law relation $\mathrm{M}_* \propto \mathrm{M}_{\mathrm{halo}}^{0.32 \pm 0.09}$. These and many other studies have explored the BCG stellar mass and halo mass relation also at varying redshifts, and have found it to be less than unity, which implies that the BCG does not grow at the same rate as the host cluster (e.g. Lidman et al., 2012).

Since in this work the BCG definition was based on the galaxy's absolute magnitude — and the galaxies' stellar mass to magnitude relation is dispersed in the lower mass end — it is reasonable to also examine how the stellar masses of the BCGs

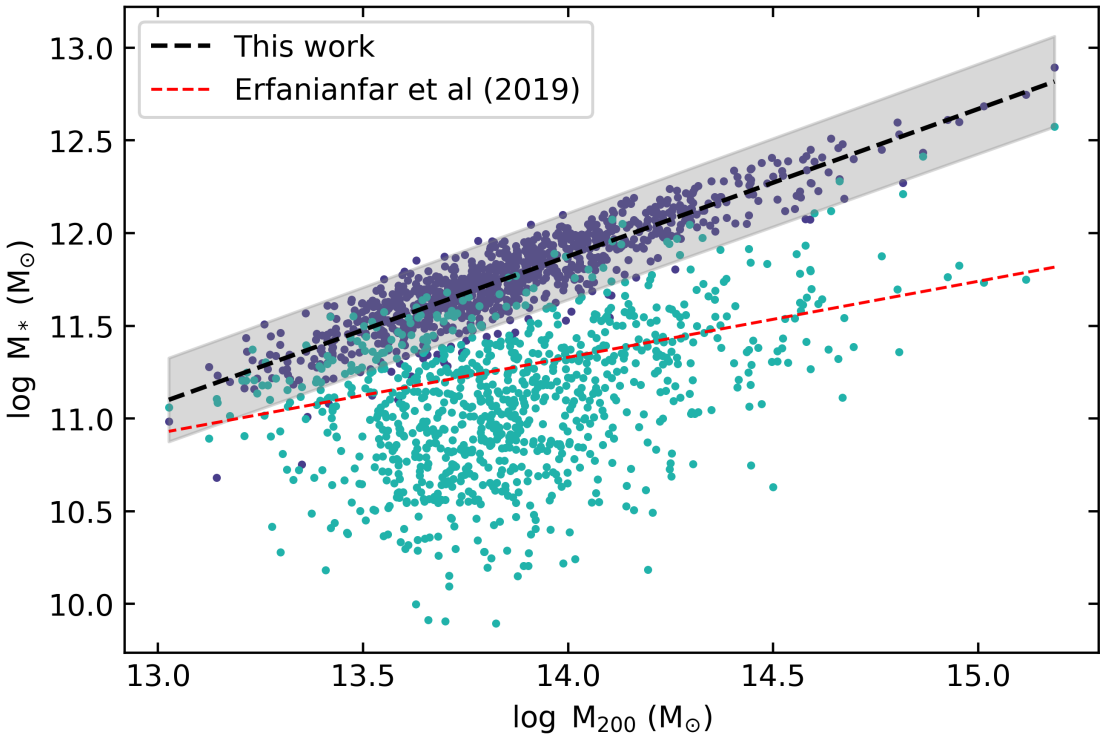

Figure 5. BCG (blue) and SBCG (green) stellar mass as a function of cluster virial mass. The black dashed line corresponds to the fit to BCG stellar mass to halo virial mass data, the error band of the linear fit is shown in light gray. A comparison with the correlation provided by Erfanianfar et al. (2019) is shown in a red dashed line.

compare to SBCGs. This distribution is seen in Figure 6. The median values for the stellar masses of BCGs and SBCGs are $10^{11.41}$ $M_\odot$ and $10^{10.78}$ $M_\odot$ respectively. As expected, in most cases the BCG is more massive than the SBCG. However, it is evident that there are 29 halos in which the SBCG is slightly more massive. For these instances, the absolute magnitudes of the brightest and second brightest galaxy are analyzed and it is found that these clusters follow a magnitude gap condition

$$M_2 - M_1 < 0.487 \text{ mag}, \tag{13}$$

where M_1 is the BCG and M_2 the SBCG absolute r-band magnitude. As will be demonstrated later in this work, other clusters tend to have magnitude gap values between 0 and 4 mag. A small magnitude gap can suggest that the system has not yet reached dynamical equilibrium, i.e., it is not a relaxed system and might still

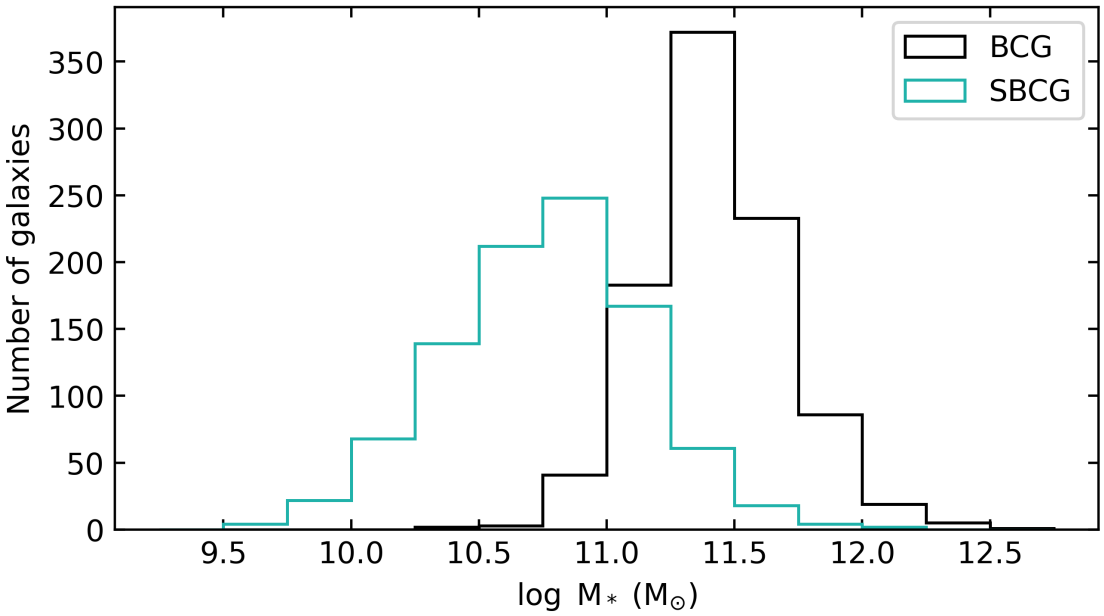

Figure 6. Stellar masses of BCGs and SBCGs. The median values of the distributions are $10^{11.41}$ $M_\odot$ and $10^{10.78}$ $M_\odot$ respectively.

be undergoing merger events. From observational data, Lopes et al. (2018) have noted that the distinction between relaxed and not relaxed (disturbed) systems can already be drawn from a magnitude gap $M_2 - M_1 = 1$ mag, meaning that these clusters are very likely disturbed systems.

4.2.2 Fossil systems

Another proxy to try to estimate if a cluster has reached dynamical equilibrium can be via identifying if they are so-called fossil systems. Fossil systems are galaxy groups and clusters whose luminosity is provided mainly by a massive central galaxy (e.g. De Oliveira et al., 2006). These objects were formed hierarchically at an early epoch in the Universe, hence why they are called fossils. These systems are assumed to have assembled half of their dark matter mass long before $z = 1$, after which the majority of growth is performed via minor mergers alone. The accretion rate of these systems should be 1/3 of what is typical for regular groups or clusters (Von Benda-Beckmann et al., 2008; Zarattini et al., 2014). The first observational definition of

fossil groups was provided by Jones et al. (2003) as follows:

i. magnitude gap $M_2 - M_1 > 2$ mag,

ii. BCG and SBCG distance $< 0.5\ R_{200}$,

iii. X-ray halo with luminosity $L_X > 10^{42}\ h_{50}^{-2}$ erg s^{-1}.

I apply the conditions i. and ii. to the TNG cluster sample for an estimation of fossil systems in the simulation. Due to there being no current available information on the halo X-ray luminosities, the last criterion was neglected. Since this criterion is only given to ensure that the system is located in a potential well that is similar in mass to a group or cluster, not considering it does not remove an important parameter as the previously set halo mass limits cover the same condition. Of the sample of 945 $z = 0$ clusters, 88 of them (9.3%) follow the fossil system criteria, indicating that only a small part of the clusters are old systems with mainly one luminous galaxy, very low accretion and effectively no star formation. Previous studies on the same topic suggest that on average the fraction of fossil systems is around $10 - 15\%$ (e.g. overview article by Aguerri & Zarattini, 2021), which is in good agreement with the TNG300 results presented here.

4.2.3 Star formation rates

A galaxy's star formation rate is related to multiple factors, including the galaxy's age and the amount of cold gas it contains. In the case of BCGs, it is expected that their specific star formation rate (sSFR), that is, the star formation rate per unit stellar mass, would be lower compared to other cluster members (Croton et al., 2006; Mo et al., 2010). This is related to the assumption given in the cluster formation, where it is supposed that due to being moved to the cluster potential minimum by dynamical friction and matter accumulating there, the BCG has gone through a rapid growth and will not have strong star formation at current time. The star

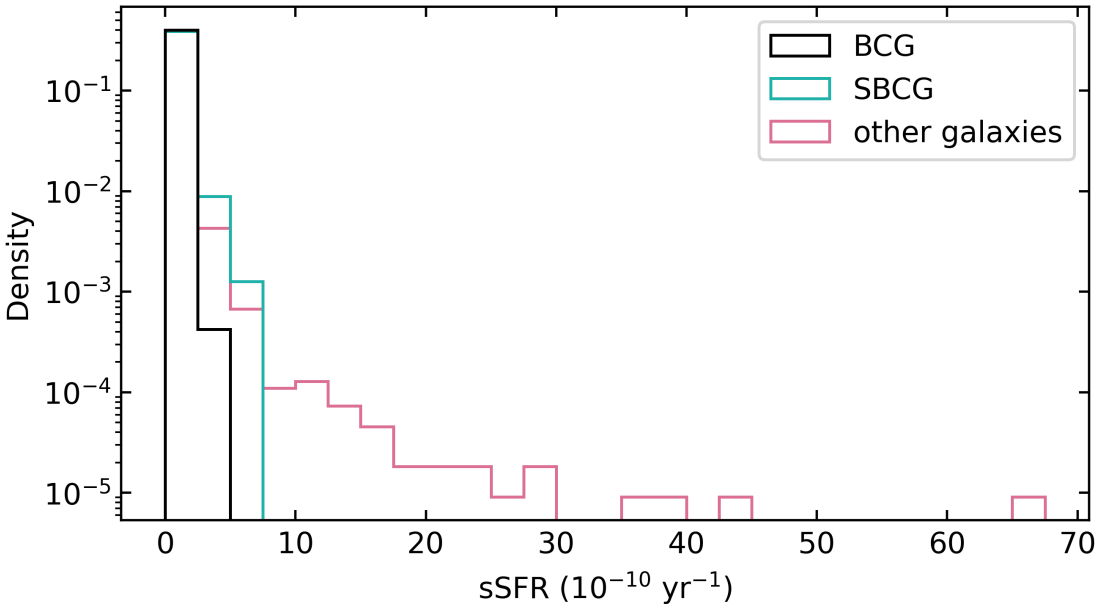

Figure 7. Distribution of specific star formation rates of the BCGs, SBCGs and remaining galaxies in the clusters.

formation rate of a galaxy can also depend on factors such as AGN feedback, which can lead to either increased or suppressed star formation, depending on the exact interactions in the vicinity of the central black hole. The TNG simulations provide a great tool for analyzing these complex interactions; however, this would be a separate study and thus is beyond the scope of this work.

The BCGs', SBCGs' and other cluster members' specific star formation rates are compared in Figure 7. It is visible that, indeed, for BCGs, the sSFR is notably smaller than that for other member galaxies in the cluster. The maximum BCG sSFR is $2.67 \cdot 10^{-10}$ yr^{-1} and the median is $4.8 \cdot 10^{-13}$ yr^{-1}. This is in good agreement with observational studies, e.g. Orellana-González et al. (2022) find the BCGs to have a sSFR between $5 \cdot 10^{-15}$ and $6 \cdot 10^{-10}$ yr^{-1}.

According to a study by Koyama et al. (2013), a galaxy is considered quiescent (i.e. no longer star-forming) at a given redshift when its sSFR satisfies the condition $\mathrm{sSFR}(z)[\mathrm{yr}^{-1}] = 10^{-10}(1+z)^3$. Based on this, all BCGs and most of the other galaxies at $z = 0$ in these systems are quiescent, meaning most of the growth has to

come from accretion of stars and mergers. This idea of cluster galaxies in general having very low star formation rates is backed up by a study by Vulcani et al. (2010), where they analyzed the influence of environment on a galaxy's star formation. The authors concluded that cluster galaxies show much lower star formation than similar mass field galaxy counterparts, indicating that the cluster environment strongly suppresses star formation.

4.3 BCG dynamical properties

Dynamical properties are the properties related to the cluster members' motion. In this section, the BCG central offsets relative to the potential well of the cluster and BCG peculiar velocities will be discussed in particular.

4.3.1 Central offsets

The offset $d_{\rm off}$ between the halo potential minimum and the center of mass of the BCG was calculated for each cluster. Similar offsets were also found for the second brightest members. Based on the central galaxy paradigm, we should see a good alignment between the BCG center of mass and the cluster potential minimum, assuming that the systems are relaxed. The distribution of the offsets is shown in Figure 8. Most BCG mass centers are located within 100 kpc of the potential minimum, with the median distance being 89.6 kpc. For SBCGs, the median distance is 830.2 kpc. The offsets can be compared with those found in observations of the BCG location relative to the cluster's X-ray peak. For instance, in De Propris et al. (2020), they find a few tens of kpc offsets for a significant fraction of BCGs. Chu et al. (2021) find that 51% of the BCGs are within a 30 kpc radius range from the X-ray center of the cluster; however, 20% of the BCGs are located farther than 100 kpc from the center. Seppi et al. (2023) note an average BCG distance of 76.3 kpc. Compared with observational results, the offsets are somewhat larger

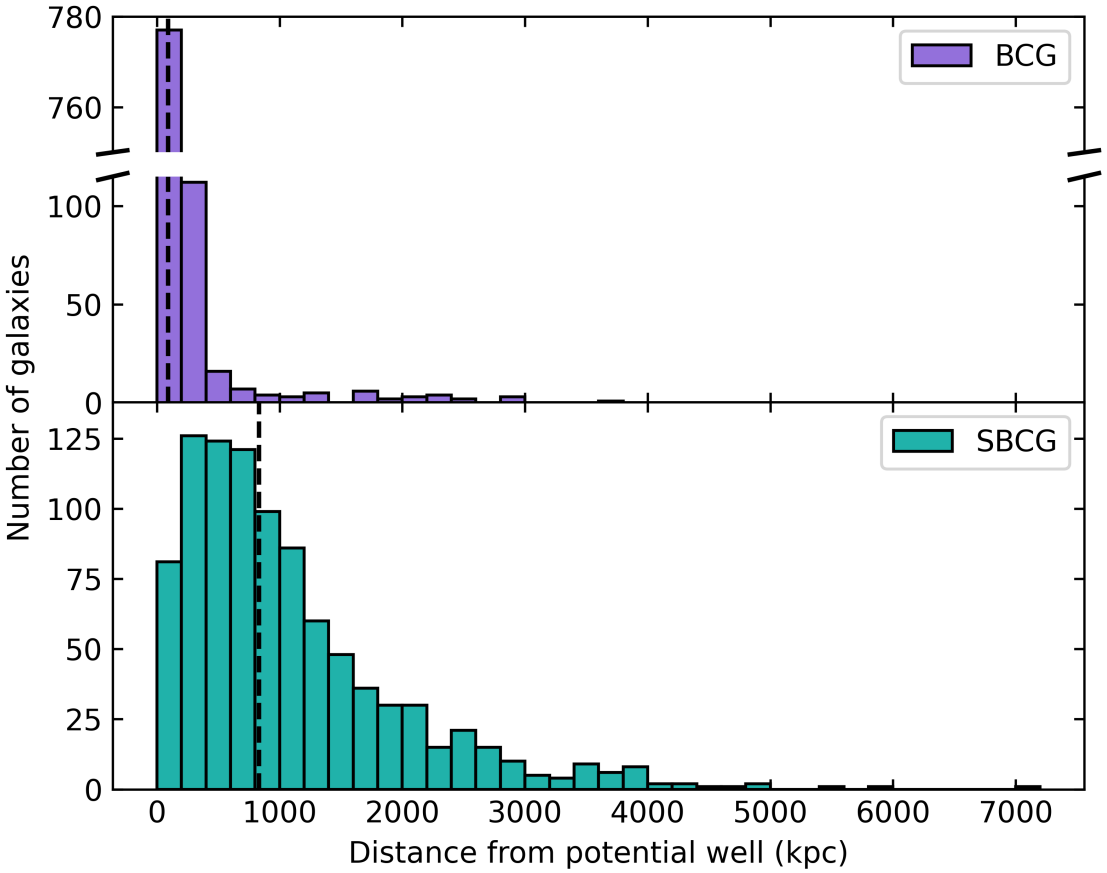

Figure 8. Distribution of BCG (top) and SBCG (bottom) distances from the potential minimum with the median value shown in a black horizontal line. The median distances are 89.6 kpc and 830.2 kpc respectively.

in the TNG300 simulation. This for one can be related to the fact that in the case of simulations, the distances are "true distances", whilst for observations it is only possible to calculate distances projected along the line of sight. When calculating the distances as a plane projection for the simulated data, there was a 24% decrease in the total distances due to projection effects. Another difference that has to be taken into account is that in this work the distances are taken between the BCG center and the potential well of the cluster; for observations, the best equivalent approximation is to find the distances from the X-ray center. In reality, there is evidence that the potential well does not always exactly coincide with the X-ray center, leading to differing offsets. The importance of choosing the cluster center

has been emphasized in multiple studies. Cui et al. (2016) note a difference between the locations of the BCG, the X-ray luminosity peak, and the minimum of gravitational potential. In their work, the center of BCG was found to correlate more strongly with the potential well than with the X-ray center. In Roche et al. (2024) they analyze how in the TNG300-1 simulation box the BCG offsets differ based on the choice of the cluster center. In their work, they also find that the estimation of the potential well as the cluster center (compared to dark matter, lensing, and gas centers) leads to the smallest BCG offsets. Additionally, the paradigm is defined under the assumption that the systems are relaxed, a condition that is not confirmed for the current data. An analysis of the clusters' dynamical state and the offset values in relaxed systems will be presented in Section 4.5.

The BCG and SBCG offset distributions were compared with those of randomly selected cluster member galaxies to assess whether the offsets of BCGs and SBCGs are statistically distinct. While the BCG offset distribution shows a clear deviation even under visual inspection, it was necessary to employ a statistical test to evaluate the SBCG distribution. The Kolmogorov-Smirnov (KS) test was chosen for this. From the entire set of galaxies, the brightest and second-brightest members were removed. After that, the galaxies were grouped by their cluster indices and from each group one random galaxy was chosen and its distance to the potential minimum was calculated. This process was done 100 times and the KS test was applied pairwise to each random distribution and the SBCG distribution. In all cases the null hypothesis of the test was rejected, meaning that the distributions of SBCG offsets differ from other member galaxies. The median p-value for a two-sided test was 0.00028 (mean 0.00078) and in case of a one-sided test, it was made certain that the SBCG offsets were smaller than the random selections. The test was also applied to the BCGs to confirm that the p-values for a two-sided test were effectively zero, and the offsets were smaller than for other galaxies.

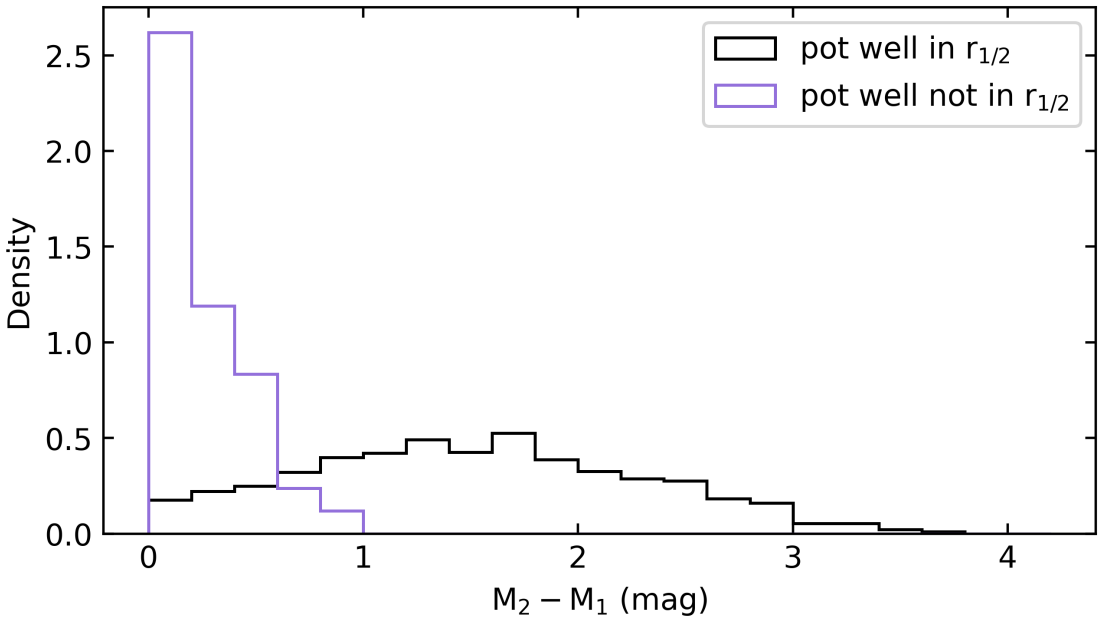

Figure 9. Magnitude gap in the case when the potential well is located within the BCG half-mass radius and when it is outside of it.

To put these distances into perspective, it is reasonable to also look at the offsets in terms of the BCGs' half-mass radius ($r_{1/2}$), i.e., the comoving radius containing half of the total mass of the BCG. This approach will give a good estimate on whether the center of the cluster's potential minimum is located somewhere within the BCG. Defining the condition

$$\frac{d_{\text{off}}}{r_{1/2}} \leq 1, \tag{14}$$

it was found that in 903 (95.5%) of the halos, the cluster's potential minimum is located within the BCG's half-mass radius. This may indicate that the system is approaching dynamical equilibrium or that the BCG might be oscillating about the potential well of the cluster. The magnitude gaps for these systems were analyzed. The purple bins in Figure 9 represent the systems in which the potential well of the cluster is not within the BCG's half-mass radius (i.e. equation 14 does not apply), and the black bins portray the case where it is within the half-mass radius. The

"not in $r_{1/2}$" situation follows a magnitude gap relation

$$M_2 - M_1 < 0.868 \text{ mag.} \tag{15}$$

This can again indicate that, in case there is a larger BCG offset, the magnitude gap tends to be smaller, therefore the system has likely not reached dynamical equilibrium and can be considered a disturbed system, as was defined by Lopes et al. (2018). The distribution for the "in $r_{1/2}$" case is considerably wider, the peak is between 1.2 and 1.8 magnitudes, and the median value is 1.51 mag. The larger magnitude gaps are typically associated with the old age and relaxation of the system, as was shown, for instance, in the previous section regarding the fossil systems. In these fossil groups, the median d_{off} is 51.7 kpc and in all cases the potential well is located within the BCG half-mass radius.

Furthermore, Kravtsov (2013) has noted that the relation between BCG sizes and virial radii of their host halos is close to linear over the entire range of stellar masses (where a power-law relation $\log r_{1/2} \propto (0.95 \pm 0.065) \log(0.015\ R_{200})$ is mentioned). In this work, the half-mass radius of the BCG correlates with its halo's virial radius (both in units of kpc) as

$$\log r_{1/2} = (0.991 \pm 0.039) \log(0.015\ R_{200}) + (1.567 \pm 0.045). \tag{16}$$

Furthermore, this can be expressed linearly as

$$r_{1/2} = (0.512 \pm 0.012)\ R_{200} + (38.91 \pm 11.00), \tag{17}$$

which corresponds well to the relation of larger (more massive) clusters hosting larger BCGs.

Moreover, it is found here that in 96.6% of the clusters, the BCG, and 52.8% cases, the SBCG is within the cluster virial radius R_{200}. This is in accordance with the hierarchical structure formation, indicating that the BCG is sinking to the potential well. On the other hand, there are 54 cases in which the SBCG is located

closer to the potential well compared to the BCG. Here, the magnitude gaps tend to differ at a greater range: $M_2 - M_1 \in [0.0017,\ 3.3235]$. The BCG offsets ($d_{\text{off}}$) also vary on a large scale, meaning there are systems where both of the two brightest galaxies are near the potential minimum as well as systems where the BCG might instead be a part of a separate substructure formed after a recent merger event. These kinds of systems are expected to still be dynamically active and show signs of high peculiar velocities.

4.3.2 Peculiar velocities

The peculiar velocities of BCGs and SBCGs are defined as the velocities relative to the motion of the cluster (i.e. the velocity differences) along all three dimensions. The total velocities are found as scalar sums $v = \sqrt{v_x^2 + v_y^2 + v_z^2}$. The average and median values for BCG peculiar velocities were 71.2 km/s and 38.5 km/s respectively, which is similar to the result obtained by Diaferio et al. (1999), where they found the average to be $\sim$ 80km/s. On the other hand, De Propris et al. (2020) find a larger median peculiar velocity where the scaled value $v_{\text{BCG}}/\sigma \sim 0.26$ corresponds to around 100 to 200 km/s. In all cases, the existence of a non-zero peculiar velocity could indicate that the BCG is either moving towards the cluster potential well or oscillating about it, depending on its location within the cluster.

To get a clearer overview of these relations, the peculiar velocity of the BCG is compared with its offset from the potential minimum and the magnitude gap between the BCG and SBCG r-band magnitudes. In the velocity vs. offset relation shown in Figure 10, there is a noticeable region where after an offset of $d_{\text{off}} > 500$ kpc (vertical light gray line), the peculiar velocities have a lower limit $v_{\text{pec}} > 145$ km/s (horizontal line). The halos in this region tend to mostly be of low and intermediate mass based on the color bar shown in the figure. This peculiar velocity limit corresponds to the magnitude gap $M_2 - M_1 < 1.6$ mag, as seen in Figure 11, given with

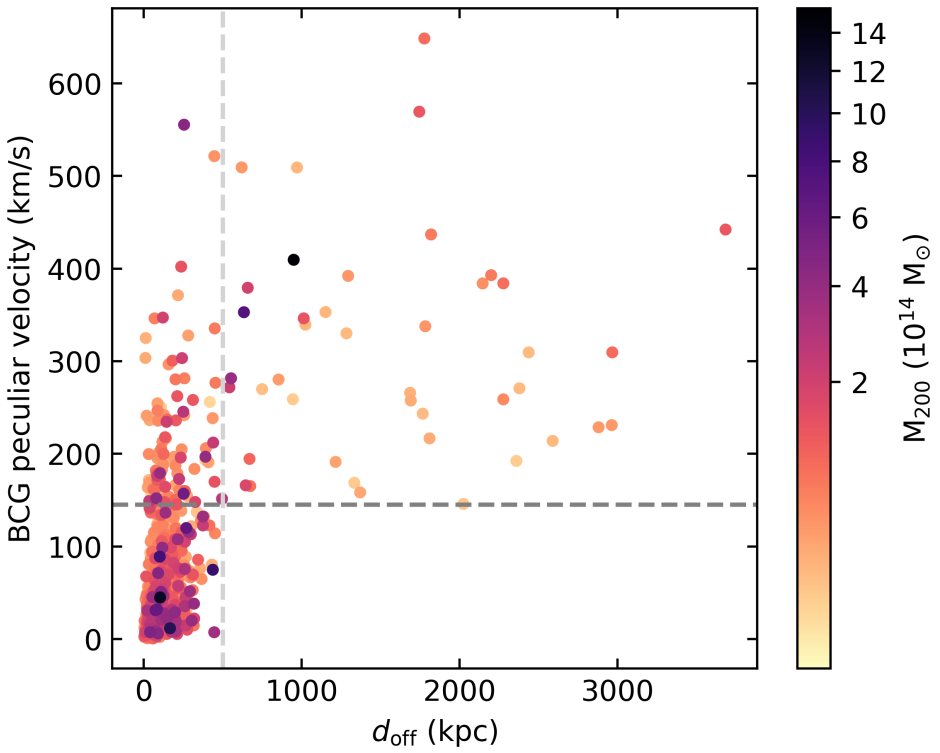

Figure 10. BCG peculiar velocity relative to the BCG offset. The color bar represents the halo virial masses. The vertical gray line is at $d_{\rm off} = 500$ kpc and the horizontal at $v_{\rm pec} = 145$ km/s.

the vertical line. This indicates that all the clusters that have a large BCG peculiar velocity have a SBCG which is at around a similar magnitude (so also a similar mass based on the galaxies' mass–magnitude relation). The large velocity can therefore be driven by the other cluster members' gravitational influence. On the other hand, the limits also form a region of mostly intermediate-to-heavy mass halos are located, that is, at the high magnitude gap and low peculiar velocity region. The clusters in this region show lower BCG offsets, again supporting the assumption that larger magnitude gaps are mostly related to relaxed systems with smaller BCG peculiar velocities. Observational data analyzed by Lauer et al. (2014) confirm a similar relation. They found that small BCG separations from the cluster center relate to smaller peculiar velocities, and larger offsets are associated with higher velocities.

In a similar manner, these relations can be analyzed for the clusters' second

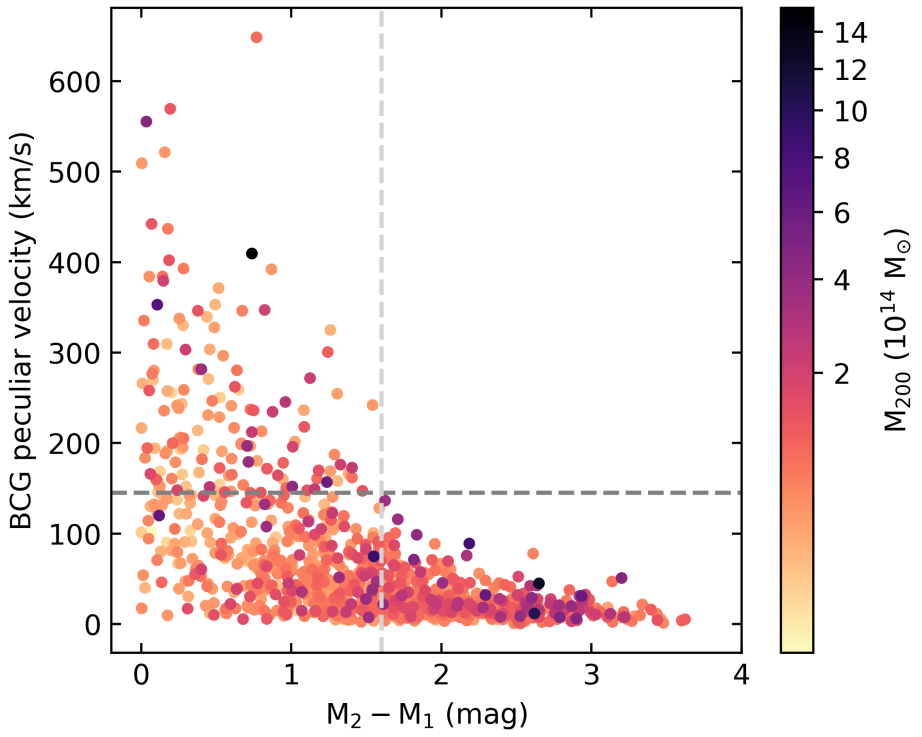

Figure 11. BCG peculiar velocity as a function of the magnitude gap. The vertical gray line is at $M_2 - M_1 = 1.6$ mag and the horizontal at $v_{pec} = 145$ km/s.

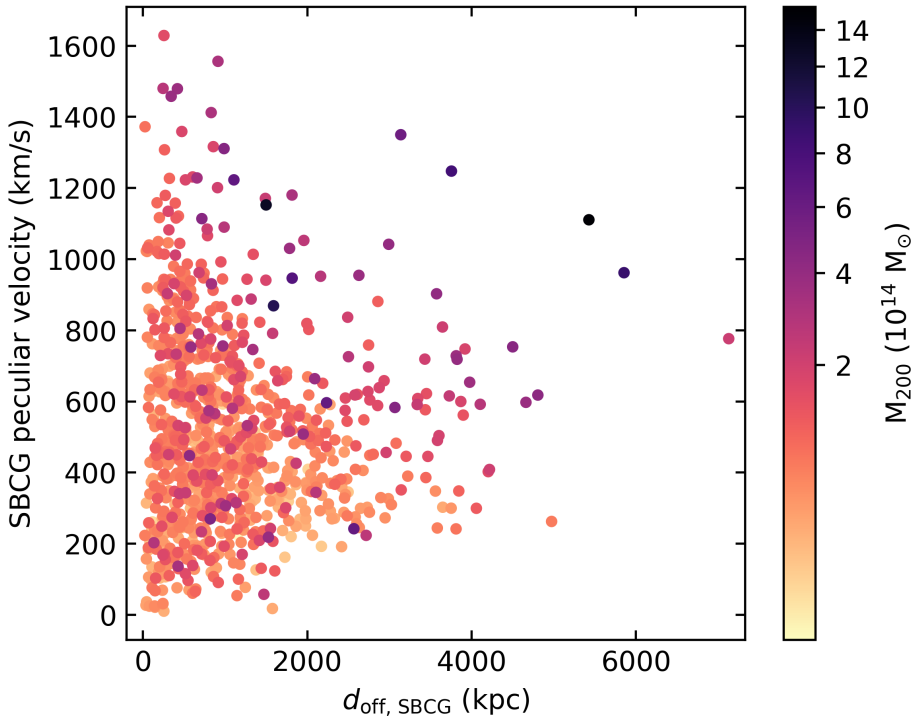

Figure 12. SBCG peculiar velocity relative to the SBCG offset.

brightest members. Figure 12 shows the peculiar velocity vs. offset relation for the SBCGs. Here, with some exceptions, more massive clusters tend to have both a larger SBCG offset and a larger peculiar velocity. This could show that in case of a more massive (and, based on the previous figures, a more likely relaxed system), the BCG is located near the cluster center while the SBCG forms a different substructure, which has a larger peculiar velocity relative to the cluster's motion. The exceptions in this case are clusters where the SBCG offset is $d_{\mathrm{off,\ SBCG}} < 2000$ kpc and peculiar velocities $v_{\mathrm{pec,\ SBCG}} > 700$ km/s. For these, the SBCG-to-BCG stellar mass ratios ($\mathrm{M}_{*,\ \mathrm{SBCG}}/\mathrm{M}_{*,\ \mathrm{BCG}}$) were found and compared to the remaining sample. The smaller distance and higher velocity SBCG systems displayed a lower mass ratio indicating that the SBCGs are notably less massive in this type of configurations. The median ratio was 0.126 (compared to 0.261 for the rest of the halos), and a KS test was used to confirm that the distributions of these two were different along with the fact that these peculiar systems were confirmed to have significantly lower values for the mass ratio.

4.4 Cluster evolution

As these galaxy systems interact with their surroundings, their properties are expected to change over time, ultimately to reach a relaxed state. In this chapter, I introduce how some different cluster characteristics, including BCG central offsets and number of substructures in the clusters, evolve with redshift.

4.4.1 Cluster substructures

Trying to explain why a cluster may not have yet reached dynamical equilibrium is a complex matter. Besides the reason possibly being that there has simply not been enough time, as typically it takes around a few Gyr for a system to relax and virialize (Poole et al., 2006), different types of ongoing dynamical interactions can prevent the system from reaching equilibrium sooner. Since galaxy clusters are typically located at the nodes of the cosmic web, where the systems are far from being isolated, interactions on different scales can occur quite regularly. Such interactions can for example be recent or upcoming cluster merger events, especially major mergers, where the mass of the counterparts is similar. Traces of these are believed to be visible in the form of distinct substructures that can be spatially separated from the rest of the cluster or have specific peculiar velocities that differ from the rest of the cluster (e.g. Ricker & Sarazin, 2001; Poole et al., 2006). To find evidence of substructures in the TNG300-1 simulation clusters, the multidimensional model-based clustering and classification algorithm *Mclust* (Fraley & Raftery, 2002; Scrucca et al., 2023) was used.

The *Mclust* package is available as open source code written in the R programming language. The algorithm is based on parameterized finite Gaussian mixture models. Models are estimated by expectation-maximization algorithm initialized by hierarchical model-based agglomerative clustering. The optimal model is then selected according to the Bayesian Information Criterion (BIC). *Mclust* has a se-

lection of 14 models with combinations of varying orientation, volume and shape. By default, the algorithm searches for the best fitting model among all the possible models, finds the optimal number of components as well as gives the classification and probability of each particle belonging to the chosen component. The uncertainty is calculated as one minus the highest probability. Since in the case of galaxy cluster data, we do not expect the substructure components to be of equal size or shape, the models with such constraints may be disregarded to save computational time. The model employed for this task was "VVI" – diagonal, varying volume and shape. In a few example cases, the goodness-of-fit (i.e. BIC) of this model was compared to all other models and gave generally the best or second best results, justifying the selection. The number of components that the algorithm was given to try modeling was between 1 and 6. This was sufficient to capture both the cases where there is no sign of distinct substructures and the cases where the cluster shows strong segmentation. The multidimensionality of the algorithm allowed me to analyze each cluster's 6-dimensional phase space data, i.e. the three spatial coordinates and peculiar velocities in the direction of each coordinate.

The analysis was done for clusters at redshifts $z = 0,\ 1$. The main purpose of this approach is to see if there are notable differences in clustering at different evolutionary steps. The fraction of the number of substructures found at each redshift is shown in Figure 13. At both redshifts, the most common number of substructures was two: 34.6% at $z = 0$ and 30.8% at $z = 1$. Additionally, it is seen that at a larger redshift, the fraction of clusters with more substructures is higher. This supports the idea of clusters moving towards dynamical equilibrium over time, where the number of detectable substructures is expected to decrease.

Next, the median magnitude gaps at both redshifts for each number of substructures were found. In Figure 14, one can see that in nearly all cases the magnitude gap is larger at $z = 0$, again supporting the idea that larger magnitude gaps are more

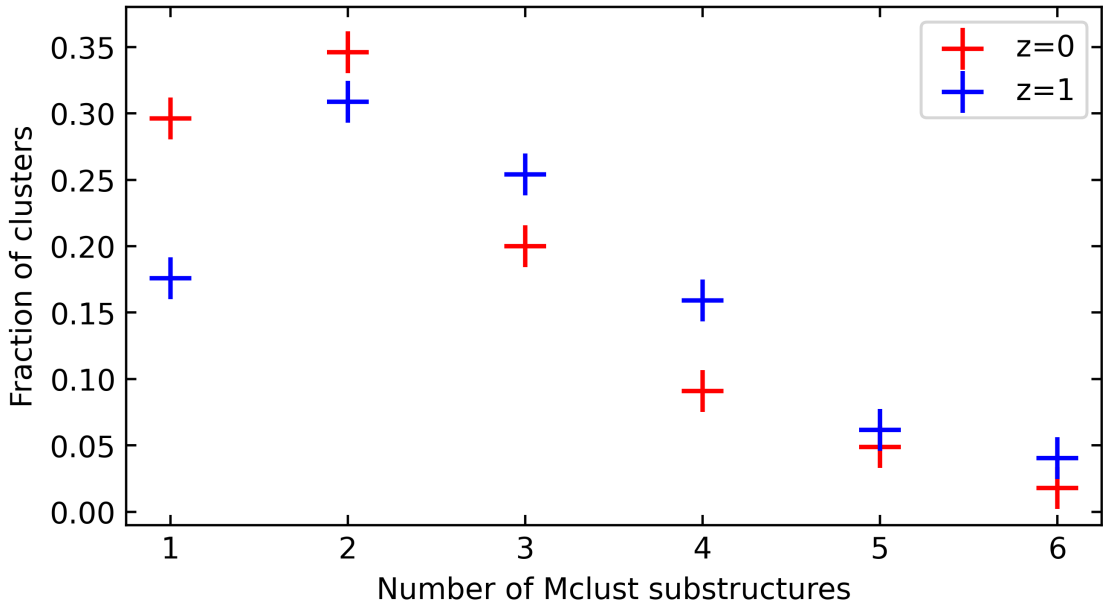

Figure 13. Fraction of substructures found with Mclust at redshifts $z = 0,\ 1$.

prevalent when systems approach equilibrium. The magnitude gap plot also shows an u-shaped configuration when going across all number of substructures at $z = 0$. This kind of relation could be associated with cluster masses, as we would expect that more massive systems are able to host more substructures. To investigate if that is the case, I find the median halo virial masses and BCG stellar masses for each substructure group. The masses are as seen in Table III. These results indicate a correlation between the number of Mclust substructures, the system masses, and the magnitude gaps (up to 4 substructures), i.e., more massive clusters tend to have more substructures, and the larger number of substructures might indicate traces of major mergers where then the BCG and SBCG of the merged system have a similar luminosity. In case of a higher number of substructures (5-6) it can be assumed that an additional bias is caused by the velocity component. It is interesting to note that although there is a correlation with cluster virial mass, no distinct correlation is observed between the number of substructures and the BCG stellar masses, meaning that BCG masses do not depend on how many other components there are surrounding it.

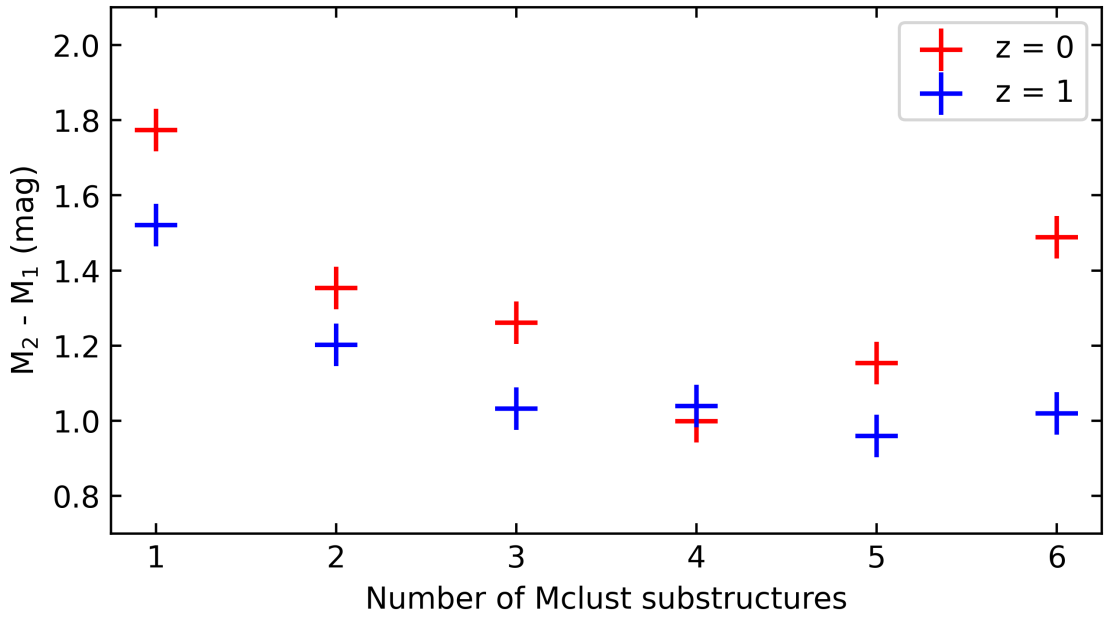

Figure 14. Median magnitude gap as a function on the number of Mclust substructures for redshifts $z = 0,\ 1$.

Table III. Median BCG stellar masses and halo virial masses for different number of Mclust substructures at redshift $z = 0$.

Substructures	1	2	3	4	5	6
$M_{*,\,BCG}$ $(10^{11}M_\odot)$	5.73	5.45	5.18	6.20	4.75	5.90
M_{200} $(10^{13}M_\odot)$	6.84	6.53	6.67	7.58	5.31	8.26

Lastly, in this section, I had a look at how the BCG and SBCG offsets and their peculiar velocities relate to the number of substructures in their host halo. The median offsets and peculiar velocities of the BCGs showed no correlation with the number of substructures, meaning that these properties are distributed similarly for clusters with a different number of substructures, causing the median value to be similar. For SBCGs at redshift $z = 0$, there was a sign of slight correlation between the offsets and number of substructures, hinting at the fact that more substructures are a result of distortions originating from cluster mergers – the initial system's BCG, after merging, has become the new system's second brightest member that

remains further from the cluster potential well due to not having sufficient amount of time to sink towards the center. The SBCG peculiar velocities didn't however correlate with the number of substructures, meaning that there is no strong relation between the SBCG velocity and where it might be located in the halo.

4.4.2 Redshift dependencies

In this section, we have a more in-depth look at the BCG properties depending on the redshift. For this analysis, redshifts $z = 0,\ 0.33,\ 0.68,\ 1$ were used. The properties are compared with the recent results obtained from the DESI Legacy Imaging Surveys and analyzed by Wen & Han (2024). The survey identified 1.58 million galaxy clusters, with 877 806 of them being found for the first time, providing the most complete observational selection to date for galaxy clusters and their brightest members up to redshifts $z \sim 1.5$.

First, the dependence of BCG central offsets was evaluated as a function of redshift. To characterize this trend, the median d_{off} was calculated at each z. The values are shown in Figure 15 on a logarithmic scale as a function of $\log(1+z)$. The data points were fit to a linear function which is described by the equation

$$\log d_{\text{off}} = (0.581 \pm 0.079)\log(1+z) + (1.963 \pm 0.016). \tag{18}$$

In the figure, it is represented by the solid red line. This shows that at higher redshifts, the BCGs tend to have larger offsets from the cluster potential well, and it is in accordance with the assumption that the clusters are moving towards dynamical equilibrium over time.

To express the dominance of a BCG in its host cluster, Wen & Han (2024) analyze how the BCG mass fraction (BCG stellar mass over total stellar mass) as a function of the cluster virial mass. To have a comparable selection of clusters, I restricted the data to $M_{500} \geq 0.47 \cdot 10^{14}\ M_{\odot}$, which was the observational limit in the DESI. For the simulation data at the four redshifts combined, I find a correlation

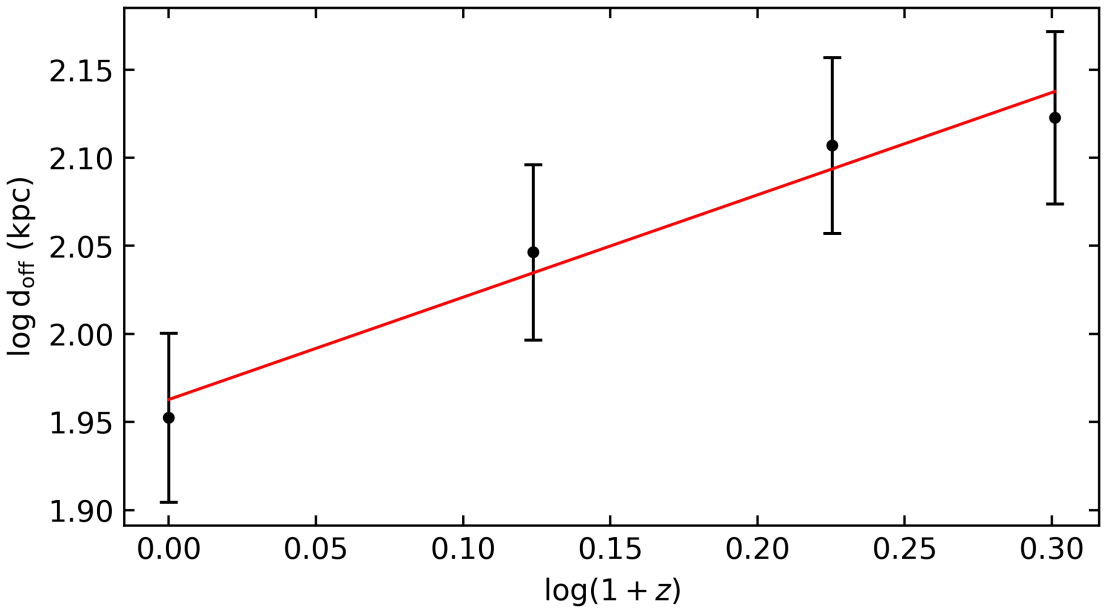

Figure 15. Median BCG offsets at different redshifts.

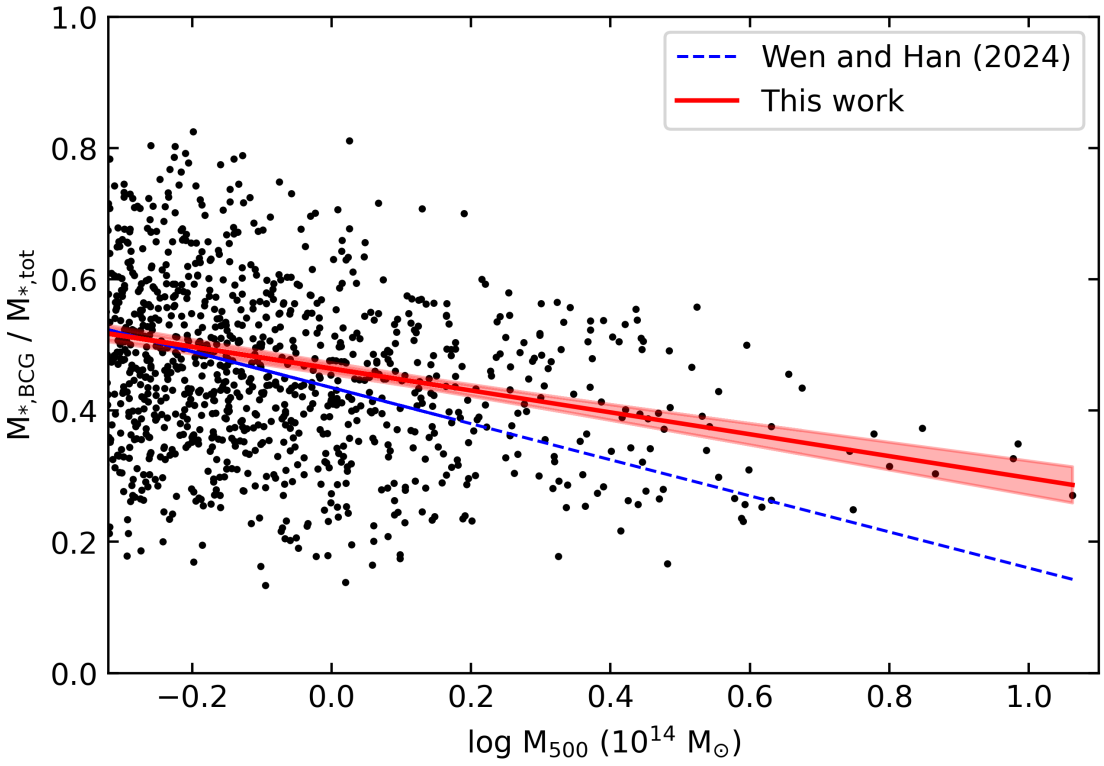

Figure 16. Fraction of BCG stellar mass among the total cluster stellar mass as a function of cluster virial mass. A linear fit to the data including an error band is shown in red. Data is restricted by cluster mass $M_{500} \geq 0.47 \cdot 10^{14}\ M_{\odot}$ to be comparable with the observational study by Wen & Han (2024).

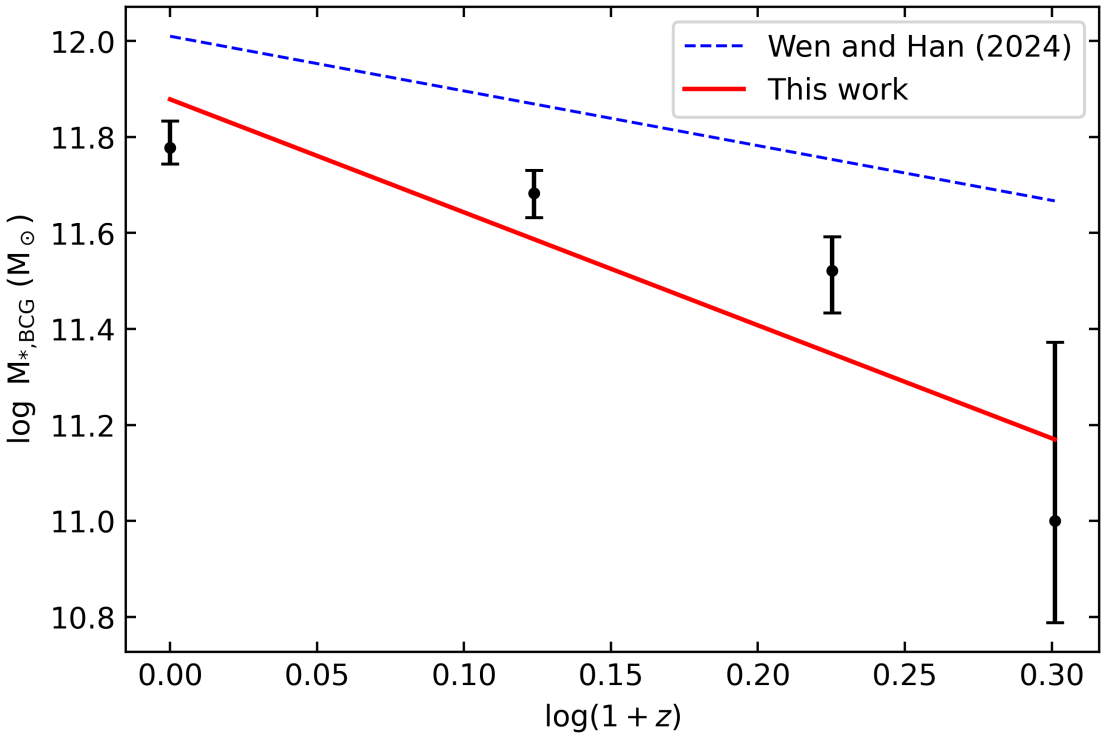

Figure 17. BCG stellar mass thresholds for keeping a constant comoving number density of BCGs across all redshifts. The reference value is taken at $z = 1$ where the minimal mass is restricted to 10^{11} $M_{\odot}$.

(solid red line in Figure 16)

$$\frac{M_{*,BCG}}{M_{*,tot}} = (0.464 \pm 0.006) - (0.167 \pm 0.025) \log M_{500} \tag{19}$$

which is quite consistent with the relation for DESI data shown with the blue dashed line in the figure. This anticorrelation indicates that BCGs are less dominant in more massive clusters which have more member galaxies.

Additionally, I analyzed how the BCG stellar mass threshold changes with redshift in the case of a constant comoving number density of BCGs. This approach is described by Wen & Han (2024) as a new way of investigating the growth of BCG stellar mass. Given that mergers between BCGs are considered negligible, the comoving number density of BCGs should be constant over time, justifying this approximation. The mass thresholds were found by applying a lower mass limit so that the number of BCGs would be the same at each redshift, in the current case it

was $n = 414$ BCGs. The reference value at $z = 1$ was taken as 10^{11} $M_\odot$ to provide comparability with Wen & Han (2024). The results are seen in Figure 17 where the red solid line represents a linear fit to the data that follows the relation

$$\log(M_{*,\mathrm{BCG}}) = (11.88 \pm 0.17) - (2.32 \pm 0.85)\log(1+z) \tag{20}$$

and the dashed blue line shows the result from DESI observations. The significant difference in the relations could be due to the fact that in their work, the authors started with the reference value at redshift $z = 0$ and extrapolated the data to find the limiting values at higher redshifts, while I started at $z = 1$ and decreased the amount of data to find the limiting values, which possibly led to a steeper slope. Here, it is also worth noting that the error values for the data at $z = 1$ are the largest, therefore future re-evaluation of the results might be necessary. Based on this relation, the growth factor for the BCG mass is found to be approximately 5 from $z = 1$ to 0, which is much higher than the results of previous studies; for example, De Lucia & Blaizot (2007) find the growth factor to be around 3, and observational studies, including Aragón-Salamanca et al. (1998) and Wen & Han (2024), result in growth factor values between 2 and 4. While a larger growth factor is in agreement with the stronger correlation between the BCG and cluster masses, as was demonstrated in Section 4.2, further analysis would be needed to draw additional conclusions about the discrepancies.

4.5 Cluster dynamical state

To apply cluster information as a measure for cosmological constraints, it is necessary to take into account the evolving dynamical state of the clusters. Most mass estimation methods assume the clusters to be relaxed systems, which often may not actually be the case due to variations mass, dynamical properties, and evolutionary stages, meaning that the relaxation is not always achieved or may be temporarily lost. So far in this study, certain approximations have been used to assume the

relaxation of clusters to explain the properties of their BCGs; here, I examine how these assumptions hold when more quantitative relaxation criteria are considered. For a cluster to be considered relaxed, Ludlow et al. (2012) suggest the following constraints:

i. subhalo mass fraction $\frac{M_{\rm sub}}{M_{200}} < 0.1$,

ii. center-of-mass shift $\frac{r_p - r_{\rm CM}}{R_{200}} < 0.07$,

iii. the virial ratio $\frac{2T}{|U|} < 1.3$.

Here $M_{\rm sub}$ is the total subhalo mass excluding the BCG mass and $r_p - r_{\rm CM}$ is the distance between the halo potential well and center of mass. In the virial ratio, the kinetic energy is expressed as $T = \sum_i \frac{1}{2} m_i v_i^2$ where v_i is the peculiar velocity of each galaxy within the virial radius and m_i is its mass. The potential energy is $U = \sum_{i,j} \frac{G m_i m_j}{r_{ij}}$, where $m_i,\ m_j$ are the masses of galaxies taken pairwise and r_{ij} is the distance between them. A more detailed discussion of choosing these criteria is provided by Neto et al. (2007), who stress the importance of using multiple objective measures to be able to reliably assess the equilibrium state of the halo. Since each of these indicators fluctuates during the virialization process, a single criterion may fail to identify out-of-equilibrium systems. However, the fluctuations of all three measures are not correlated; therefore, it is highly unlikely that all three fail at the same time (Ludlow et al., 2012).

The constraints were applied to cluster data at redshifts $z = 0$ and 1. At zero redshift, 176 (18.6%) clusters satisfy all three conditions. Within different cluster virial mass ranges, the ratios were the following:

(i) 10^{13} $M_\odot \leq$ $M_{200} < 10^{13.5}$ $M_\odot$: 1.1%,

(ii) $10^{13.5}$ $M_\odot \leq M_{200} < 10^{14}$ $M_\odot$: 20.0%,

(iii) 10^{14} $M_\odot$ $\leq M_{200} < 10^{14.5}$ $M_\odot$: 21.6%,

(iv) $10^{14.5}$ $M_\odot \leq M_{200}$: 20.5%,

which show that this condition holds best for more massive clusters and around 1/5 of them are relaxed. At $z = 1$ only 4 (0.95%) clusters follow the same criteria, with all of them belonging to the mass range $10^{13.5}$ $M_\odot \leq M_{200} < 10^{14}$ $M_\odot$. The relaxation should insist that peculiarities such as BCG central offsets, large peculiar velocities, and strong signs of substructuring are no longer observed. Due to the amount of data remaining after filtering, further analysis was performed only for the clusters at $z = 0$.

Under further inspection of each relaxation criterion, the first, regarding the relation M_{sub}/M_{200}, did not play a role in the filtering of the clusters in this data set. This would mean that taking only the mass relations into account would determine all clusters to be relaxed. The other two constraints showed more systems to be out of equilibrium. The two properties are plotted against each other in Figure 18, where the dashed lines refer to the limits given by Ludlow et al. (2012). The final region of halos that follow all the criteria is highlighted in the figure's lower left corner.

For the relaxed clusters, the maximum BCG offset d_{off} is now 145.3 kpc and the median value has decreased from the initial 89.6 kpc to 37.48 kpc, which is better in accordance with the observational results provided by De Propris et al. (2020) and Chu et al. (2021) as mentioned in Section 4.3.1. The maximum BCG peculiar velocity is 71.18 km/s, but the majority of the BCGs have a peculiar velocity that is under 14.5 km/s. In two instances, it is observed that the SBCG is located closer to the potential well than is the BCG. These peculiar systems show large mass and magnitude gaps between the two brightest members ($M_{tot,\,BCG} - M_{tot,\,SBCG} \sim 9 \cdot 10^{13}$ $M_\odot$, $M_2 - M_1 \sim 3$ mag), indicating that the BCG is much brighter and much more massive than the other members of this system. Additionally, the distance between the two brightest members is noted to be around ten times smaller than the given BCG half-mass radius. The SBCG peculiar velocities are rather large: 1372.2 km/s in

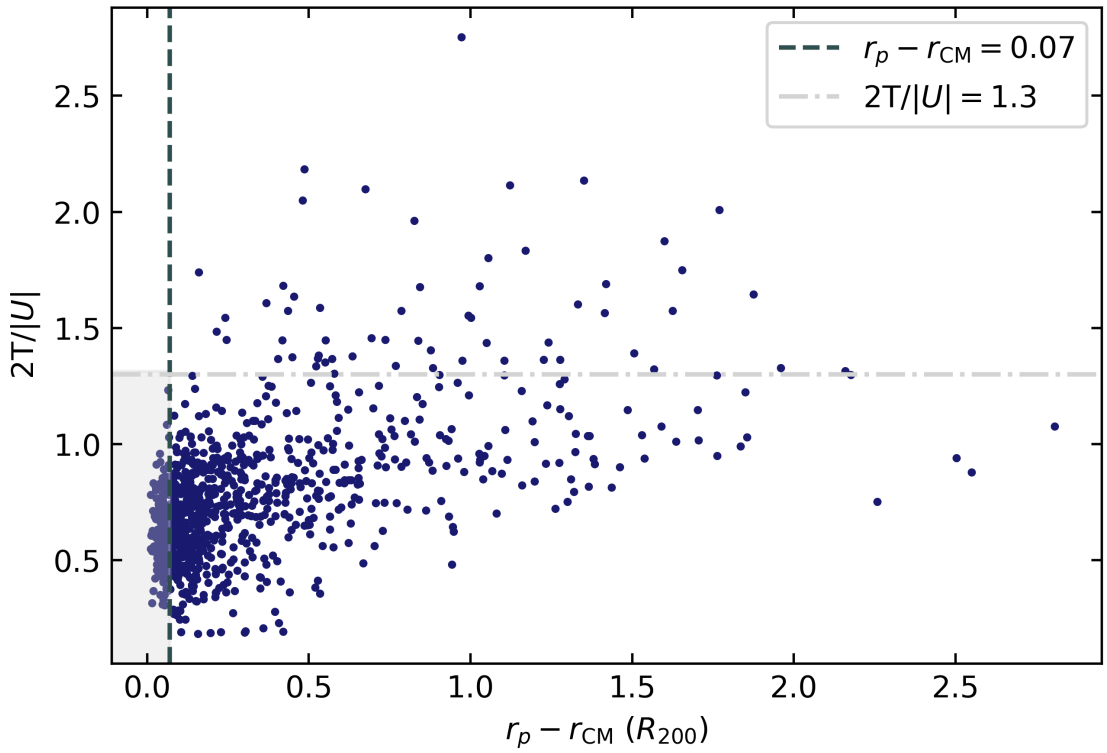

Figure 18. Selection criteria for cluster relaxation. The vertical dashed line represents the potential well and mass center distance limit, and the horizontal line the energy ratio. The final sample of relaxed clusters (176) is highlighted.

one system and 223.1 km/s in the other, which could hint at the possibility of the SBCG just coincidentally being located closer to the potential well at the current epoch. All in all, these properties imply that the two brightest members may be undergoing a merger event in the near future, or interactions between the two galaxies might already have taken place. A more detailed dynamical history analysis of these systems is however out of the scope of this work.

Additionally, I analyze how the BCG and its host cluster mass relations change under the relaxation criteria. The BCG stellar mass vs. halo virial mass takes the form:

$$\log \mathrm{M}_* = (0.781 \pm 0.027) \log \mathrm{M}_{200} + (0.996 \pm 0.377), \tag{21}$$

which is similar to the relation in the previous case expressed with equation (12). In this case, the limiting mass of the halos is around $\mathrm{M}_{200} \geq 10^{13.5}$ $\mathrm{M}_\odot$ (which cor-

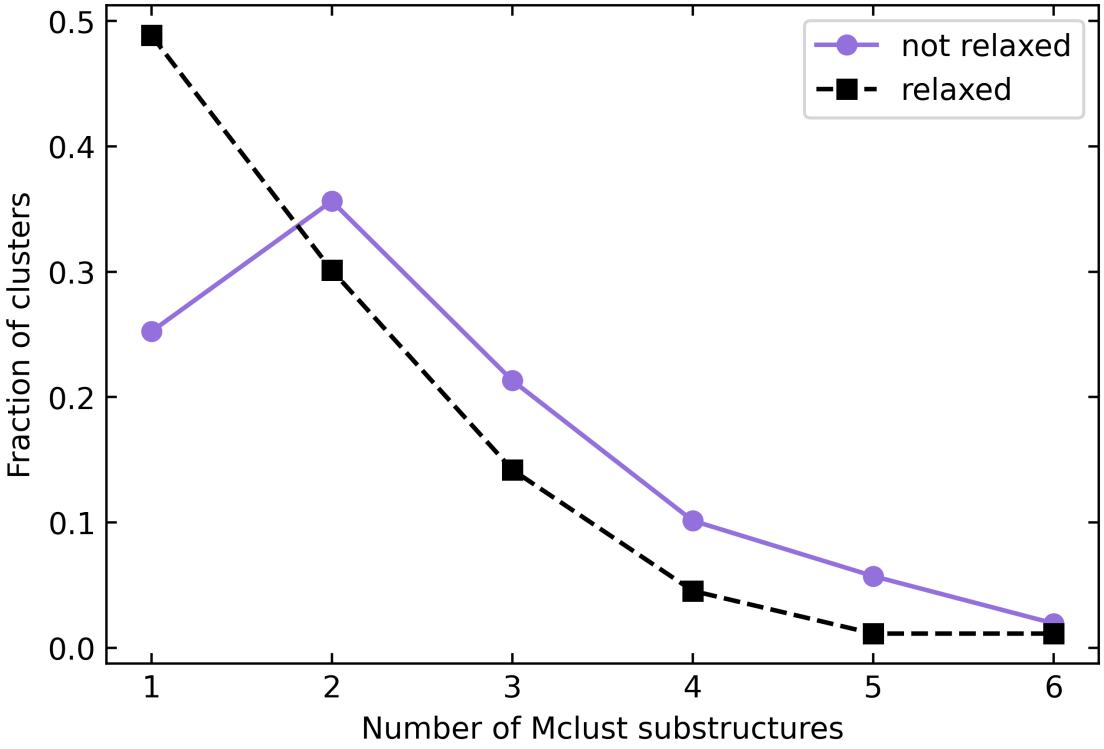

Figure 19. Fraction of substructures in relaxed (black) and unrelaxed halos (purple).

responds to BCG stellar mass of $M_* \geq 10^{11.23} M_\odot$), insisting that there could be an observationally applicable lower limit that could give an estimate of whether or not the halo could be relaxed. When comparing BCG stellar masses to SBCG masses, it becomes evident that there exists no halo where the SBCG is more massive; therefore, the BCG definition can now also be considered to be consistent with studies where the galaxy mass was used to define the BCG. Another parameter that was previously associated with relaxation is the magnitude gap – when applying the criteria, mostly only halos with a large gap remain. The median value is 2.32 mag and of all 176, only one cluster has a gap below 0.9 mag. Regarding the assumption that old fossil groups have reached dynamical equilibrium and therefore are considered relaxed, only 52.3% of them follow all three relaxation criteria, that is, 26.1% of the relaxed clusters are fossil systems.

The second relaxation criterion – the center-of-mass shift – is a statistic for mea-

suring major deviations from symmetry in the cluster mass distribution (Crone et al., 1996). Applying this should therefore eliminate systems with strong substructuring; hence, I investigate how this criterion correlates with the number of substructures previously found by *Mclust*. The normalized number of substructures for relaxed and unrelaxed clusters is shown in Figure 19. The trend indicates that the relaxation criteria lead to preferring clusters with little to no substructuring. In case of systems with no substructures, the median magnitude gap values are 2.4 and 1.6 for relaxed and not relaxed systems accordingly, leading to once again confirming that the magnitude gap has a strong correlation with cluster relaxation. It should also be noted that although the fraction of clusters with a large number of substructures has decreased, there are still a few cases where the number of substructures is large even though the cluster is considered to be "symmetric" and relaxed. This can be due to *Mclust*'s sensitivity towards the velocity component, meaning that the algorithm often finds substructures within substructures due to their slightly different velocity. So, even though the system is spatially symmetric, there are traces of possible past interactions within the cluster.

The results of applying these theoretical limitations to the simulation data can give us an estimate of the observational parameters that can be used to determine whether the clusters in the sample have reached dynamical equilibrium. This proxy can help use observational data to, in turn, compare the measures of cosmological constraints provided by different approaches. As mentioned previously, a lower halo mass limit $M_{200} = 10^{13.5}\ M_{\odot}$ (corresponding to $M_{*} = 10^{11.23} M_{\odot}$) can be determined for finding at least 20% of the halos to be relaxed and this fraction is quite consistent throughout the higher mass range. For the magnitude gap relation, the probability of observing a relaxed cluster with a certain magnitude gap is seen in Figure 20. Here, it can be noted that even though 99.4% of the relaxed clusters had a magnitude gap greater than 0.9 mag, a higher certainty of assuming the cluster to be relaxed is

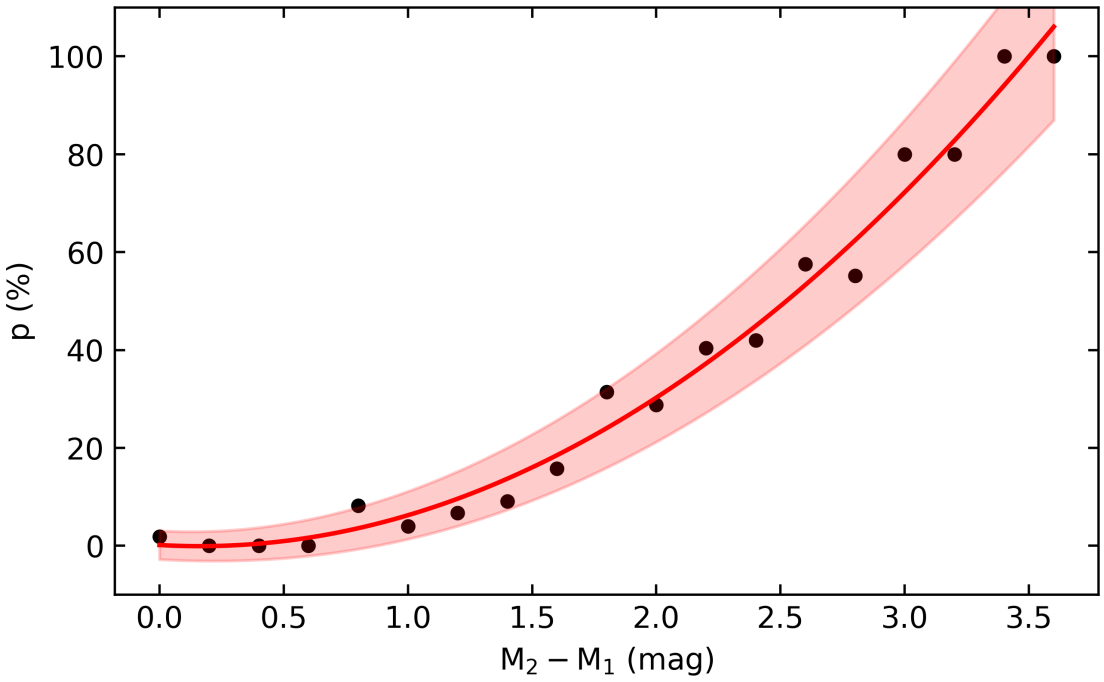

Figure 20. Probability of the cluster being relaxed at certain magnitude gap values. The data is binned by steps of 0.2 mag and the error band provided by the fit is shown in red.

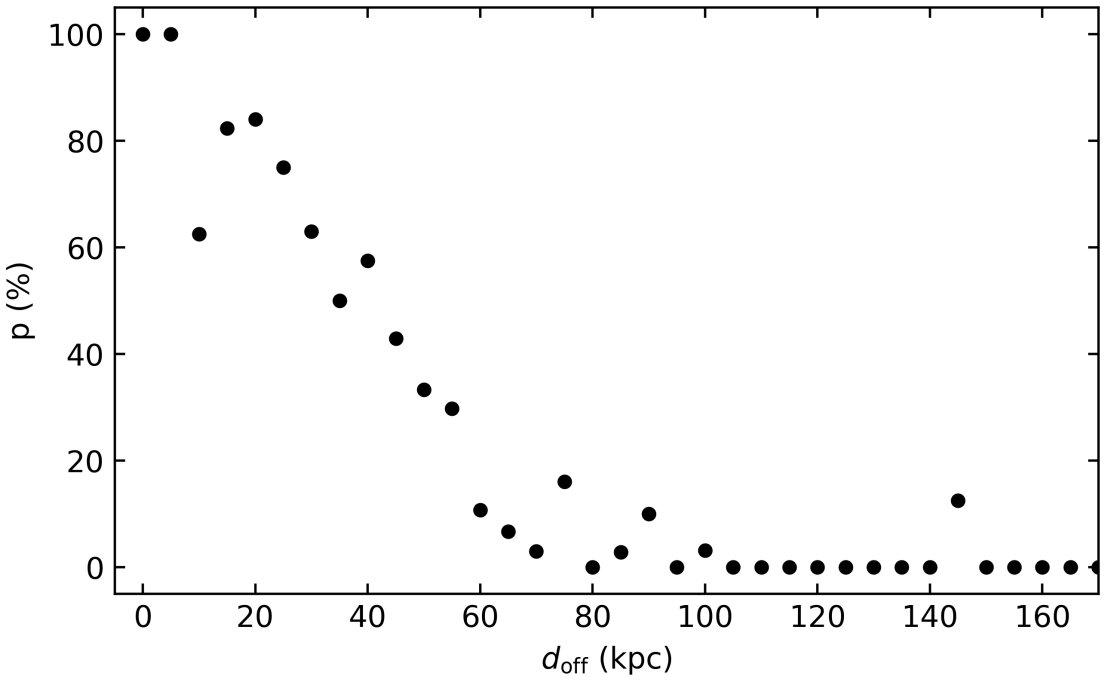

Figure 21. Probability of the cluster being relaxed at certain BCG central offset values. The data is binned by steps of 5 kpc and at distances larger than 150 kpc, the probability remains zero.

possible only at larger magnitude gaps. The probabilities follow a quadratic relation

$$p = (0.089 \pm 0.010)(\mathrm{M}_2 - \mathrm{M}_1)^2 - (0.029 \pm 0.038)(\mathrm{M}_2 - \mathrm{M}_1) + (0.002 \pm 0.029), \quad (22)$$

which is shown with a red line in the figure. Similar probabilities are calculated for the BCG central offsets. There it became evident that up to around 40 kpc, the probability of the system being relaxed is greater than 50% and that no BCGs are located beyond 150 kpc. This relation is visible in Figure 21.

Since these properties as standalone indicators are not able to well represent the dynamical state of the cluster, I evaluate these variables as a combination to find a reliable threshold for predicting a cluster's relaxation. For this, I use a Logistic Regression based machine learning algorithm, available as a Python *sklearn* package. Logistic Regression is a predictive statistical model that allows the use of a combination of independent variables to predict the probability of an event belonging to a binary class – in this case, either 1 for a relaxed, or 0 for a non-relaxed cluster. The probability of the event belonging to class 1 is determined by the relation

$$\ln \frac{p}{1-p} = \beta_0 + \sum_{i=1}^{n} \beta_i x_i, \quad (23)$$

where in this instance $n = 3$ (BCG offset, magnitude gap and BCG stellar mass). The coefficients β_i characterize the weights of each parameter x_i and β_0 is the intercept of the sigmoid function. During training, the model uses a method known as maximum likelihood estimation to find the values of the coefficients that best fit the training data. Specifically, it adjusts the weights β_i to maximize the likelihood that the predicted probabilities match the actual binary labels in the training set. When using the 'lbfgs' solver (which is the default optimization algorithm of the Python package), the optimization is carried out using an efficient gradient-based method. To avoid overfitting and improve generalization, the algorithm penalizes large coefficients. The penalty term in this function by default is 'L2', which adds a penalty proportional to the square of the model coefficients (weights) $\sim \lambda \sum_i \beta_i^2$, where λ is the regularization strength hyperparameter.

To assess whether this model is actually capable of adequately predicting cluster relaxation based on the three input parameters, I evaluated its performance using standard classification metrics such as accuracy, precision, and recall. This was done through supervised learning, where, in short, the model is trained on labeled data – clusters with known dynamical states – and then it is tested on data without knowing the true class to evaluate generalization. Specifically, I used cross-validation, where the sets were randomly chosen for each run in which 80% of the data was used to train the algorithm and the remaining 20% was used for testing. The test score values over 10 runs were as follows:

$$\text{accuracy} = \frac{TP + TN}{\text{total}} = 90.7\%,$$

$$\text{precision} = \frac{TP}{TP + FP} = 77.6\%,$$

$$\text{recall} = \frac{TP}{TP + FN} = 72.2\%,$$

where TP, TN, FP, FN are the true positive, true negative, false positive and false negative classification rates accordingly. These can be considered sufficient performance values to estimate the probabilities based on these metrics. The weight coefficients for each parameter were assigned by the model as: $\beta(d_{\text{off}}) = -0.072$, $\beta(\text{M}_2 - \text{M}_1) = 0.941$ and $\beta(\log \text{M}_*) = 2.429$, the average intercept was $\beta_0 = -27.6$. It is important to note that the input parameters in this case were not standardized; therefore, the given weights also reflect the size scales of these values. Following this model, the probabilities given by the combinations of varying the three parameters were analyzed. Firstly, it was noted that multiple points in the parameter space have similar relaxation probabilities; this means, for instance, if the BCG central offset is very small, the magnitude gap and BCG mass are also allowed to be slightly smaller. These relations are depicted in Figure 22, where the color represents the probability, and the lower threshold is $p \sim 0.7$. For a better visual representation of this, the relaxation probabilities are taken as medians over different BCG stellar mass bins,

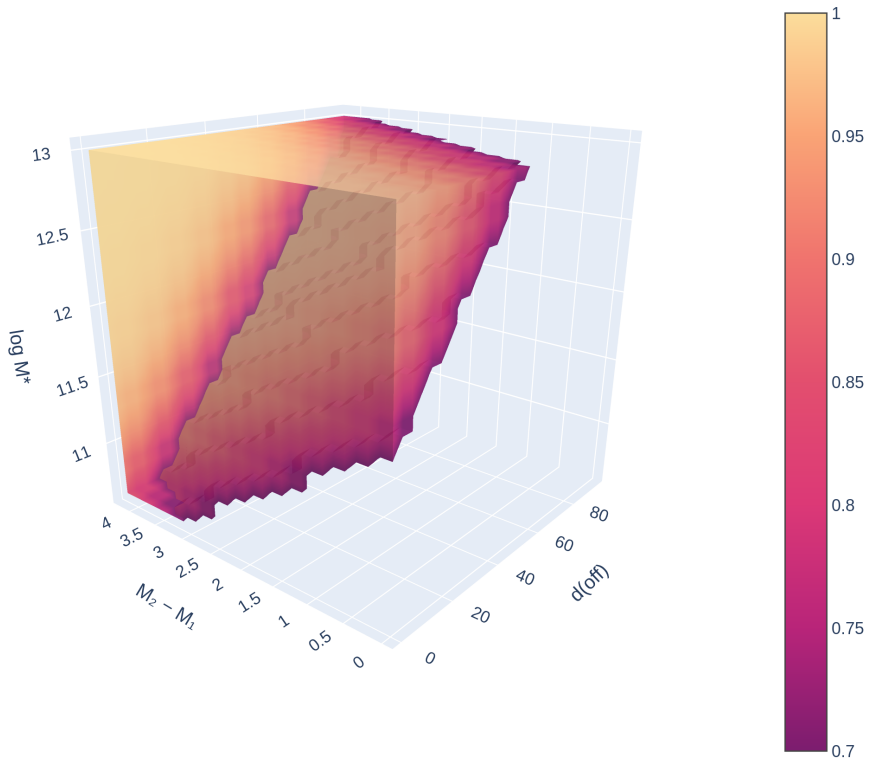

Figure 22. 3D parameter space of observable cluster properties. The probability of the cluster being in dynamical equilibrium is represented with the color bar, the lower threshold is chosen as $p \sim 0.7$.

as shown in Figure 23. For each BCG offset and magnitude gap combination, the probability is indicated with the color given by the color bar. Similarly as for the 3D figure, it can be noticed that in the case of larger masses, the other two parameters can vary on larger scales, meaning there is no one fixed value for each property, but rather a combination of equal probabilities in the parameter space that have to be accounted for simultaneously.

This result provides a set of observable parameters that can be used to make first estimations about the cluster dynamical state. While the majority of relaxed clusters show values $M_* \geq 10^{11.23}$ $M_\odot$, $d_{\rm off} \leq 40$ kpc and $M_2 - M_1 \geq 0.9$ mag, the probability of the cluster being relaxed is given by the location in the 3D parameter space and can be applied to observational data when identifying the cluster potential minimum as the observed X-ray emission peak, as this is the best current

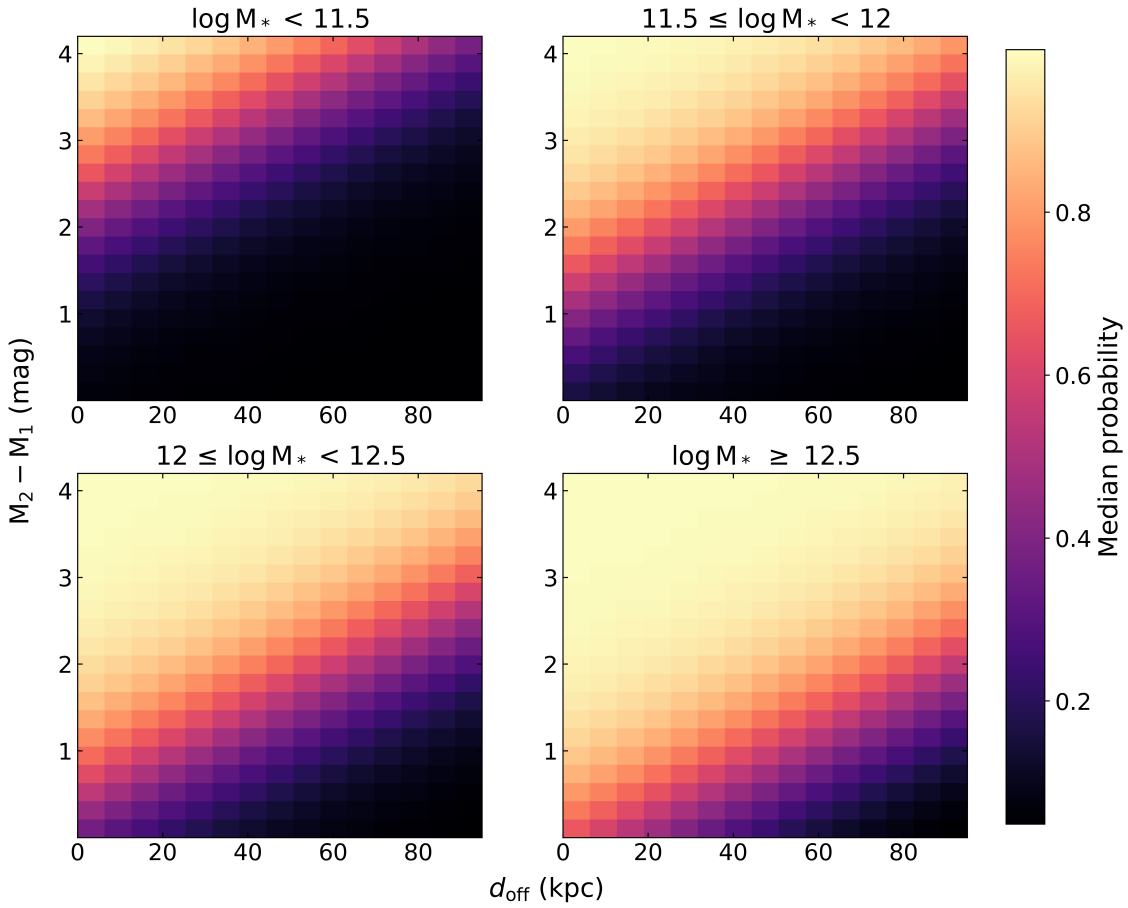

Figure 23. Median probability of the cluster being in dynamical equilibrium for each BCG central offset – magnitude gap combination in different BCG stellar mass bins.

observational approximation for the cluster center.

5 Summary

This work has shown how the properties of BCGs in the IllustrisTNG simulation relate to their host environment. The size and mass relations of the BCG and its host cluster show strong correlations, indicating that the growth of the structures is strongly tied, as is expected from hierarchical structure formation. Regarding the central galaxy paradigm, the BCG mass centers are generally found to be located close to the cluster potential well with a median distance of 89.6 kpc, additionally it was noted that in 95.5% of the cases, the BCG center-of-mass distance from the potential well was smaller than the BCG half-mass radius, indicating that the systems would be moving toward dynamical equilibrium. The peculiar velocities of the BCGs and SBCGs displayed subsets of clusters where, when the BCG showed a large peculiar velocity – the magnitude gap between the two brightest members was noted to be small, implying that the dynamics of the BCG might be strongly influenced by other cluster members and that there could be a possibility of similar mass substructures within the cluster. Substructuring within the clusters at redshifts $z = 0,\ 1$ was analyzed with *Mclust*. In both cases, the most common number of substructures (in $\sim 1/3$ of clusters) was found to be 2. The median magnitude gap in this case did not strongly depend on substructuring, as the number of substructures was also dependent on the size (mass) of the cluster. Cluster evolution was also taken into account and compared to a recent observational study by Wen & Han (2024). The results from this analysis support the idea of clusters moving towards dynamical equilibrium over time, since the BCG distance from the halo center decreases when approaching the current epoch. Additionally, in more massive halos, the BCG is shown to be less dominant over other cluster members.

Lastly, given that these measures often led to estimations of whether the cluster could be dynamically relaxed or not relaxed based on different properties, three quantitative dynamical state constraints were used to determine how these proper-

ties actually behave in relaxed clusters. The three criteria showed that in the current epoch, around 20% of the clusters with mass $M_{200} \geq 10^{13.5}$ $M_{\odot}$ are in dynamical equilibrium. In these clusters, properties such as the BCG central offsets and peculiar velocities notably decreased, while the magnitude gap increased, supporting the previous dynamical state assumptions. Since these criteria also take the symmetry of the cluster into account (via the center-of-mass shift), the fraction of clusters with no substructuring increased notably, however, a few clusters with a higher number of substructures also remained, indicating that even relaxed systems can show traces of past interactions in their 6D phase-space. Moreover, it was shown that it is possible to quite well predict a cluster's dynamical state based on three observable properties: the magnitude gap, BCG stellar mass, and BCG offset. Combining these into a 3D parameter space allows one to filter observational data more easily, leading to a reliable set of clusters based on which cosmological constraints can be applied without falsely assuming dynamical equilibrium.

This study focused mainly on the higher mass end of these gravitationally bound systems known as galaxy clusters. As a future outlook, it will be important to expand the analysis to the lower mass end of galaxy groups and brightest group galaxies, which have so far not been studied in detail due to instrumental limitations. In my future work, this topic will be studied using the same current simulation while restricting the group mass below $10^{13.5}$ $M_{\odot}$, which was the limit found for relaxed galaxy clusters. As the instrumentation in the observational field advances, more specific measurements of these properties will become feasible, leading to better comparisons of theoretical data with observational. As of the beginning of 2026, with the commencement of the 4MOST (4-metre Multi-Object Spectroscopic Telescope) observations, higher-fidelity data will become available for galaxy groups and brightest group galaxies, providing the opportunity to connect observations and simulations into one comprehensive project.

References

Aguerri J. A. L., Zarattini S., 2021, Universe, 7, 132

Allen S. W., Evrard A. E., Mantz A. B., 2011, ARA&A, 49, 409

Aragón-Salamanca A., Baugh C. M., Kauffmann G., 1998, MNRAS, 297, 427

Biffi V., Dolag K., Böhringer H., 2013, MNRAS, 428, 1395

Binney J., 1977, ApJ, 215, 483

Brinchmann J., Charlot S., White S. D. M., Tremonti C., Kauffmann G., Heckman T., Brinkmann J., 2004, MNRAS, 351, 1151

Chu A., Durret F., Márquez I., 2021, A&A, 649, A42

Chu A., Sarron F., Durret F., Márquez I., 2022, A&A, 666, A54

Cole S., Lacey C. G., Baugh C. M., Frenk C. S., 2002, MNRAS, 319, 168

Crone M. M., Evrard A. E., Richstone D. O., 1996, ApJ, 467, 489

Croton D. J., et al., 2006, MNRAS, 365, 11

Cui W., et al., 2016, MNRAS, 456, 2566

Dalal R., Strauss M. A., Sunayama T., Oguri M., Lin Y.-T., Huang S., Park Y., Takada M., 2021, MNRAS, 507, 4016

Davis M., Efstathiou G., Frenk C. S., White S. D. M., 1985, ApJ, 292, 371

De Lucia G., Blaizot J., 2007, MNRAS, 375, 2

De Oliveira C. L. M., Cypriano E. S., Sodré Jr. L., 2006, AJ, 131, 158

De Propris R., et al., 2020, MNRAS, 500, 310

Diaferio A., Kauffmann G., Colberg J. M., White S. D. M., 1999, MNRAS, 307, 537

Dressler A., et al., 1997, ApJ, 490, 577

Einasto M., Einasto J., Tenjes P., Korhonen S., Kipper R., Tempel E., Liivamägi L. J., Heinämäki P., 2024, A&A, 681, A91

Erfanianfar G., et al., 2019, A&A, 631, A175

Faltenbacher A., Diemand J., 2006, MNRAS, 369, 1698

Fraley C., Raftery A. E., 2002, JASA, 97, 611

Galárraga-Espinosa D., Aghanim N., Langer M., Gouin C., Malavasi N., 2020, A&A, 641, A173

Haarsma D. B., et al., 2010, ApJ, 713, 1037

Hou A., Parker L. C., Harris W. E., Wilman D. J., 2009, ApJ, 702, 1199

Jones L. R., Ponman T. J., Horton A., Babul A., Ebeling H., Burke D. J., 2003, MNRAS, 343, 627

Kauffmann G., White S. D. M., Guiderdoni B., 1993, MNRAS, 264, 201

Koyama Y., et al., 2013, MNRAS, 434, 423

Kravtsov A. V., 2013, ApJ, 764, L31

Kravtsov A. V., Borgani S., 2012, ARA&A, 50, 353

Kravtsov A. V., Vikhlinin A. A., Meshcheryakov A. V., 2018, Astron. Lett., 44, 8

Lauer T. R., Postman M., Strauss M. A., Graves G. J., Chisari N. E., 2014, ApJ, 797, 82

Lidman C., et al., 2012, MNRAS, 427, 550

Lopes P. A. A., Trevisan M., Laganá T. F., Durret F., Ribeiro A. L. B., Rembold S. B., 2018, MNRAS, 478, 5473

Ludlow A. D., Navarro J. F., Li M., Angulo R. E., Boylan-Kolchin M., Bett P. E., 2012, MNRAS, 427, 1322

Marini I., et al., 2021, MNRAS, 507, 5780

Mo H., van den Bosch F., White S., 2010, Galaxy Formation and Evolution. Cambridge University Press

Nelson D., et al., 2015, Astron. Comput., 13, 12

Nelson D., et al., 2018, COMPAC

Neto A. F., et al., 2007, MNRAS, 381, 1450

Oliva-Altamirano P., et al., 2014, MNRAS, 440, 762

Orellana-González G., Cerulo P., Covone G., Cheng C., Leiton R., Demarco R., Gendron-Marsolais M.-L., 2022, MNRAS, 512, 2758

Oser L., Ostriker J. P., Naab T., Johansson P. H., Burkert A., 2010, ApJ, 725, 2312

Pillepich A., et al., 2018, MNRAS, 475, 648

Planck Collaboration et al., 2016, A&A, 594, A13

Planck Collaboration et al., 2020, A&A, 641, A6

Poole G. B., Fardal M. A., Babul A., McCarthy I. G., Quinn T., Wadsley J., 2006, MNRAS, 373, 881

Rees M. J., Ostriker J. P., 1977, MNRAS, 179, 541

Ricker P. M., Sarazin C. L., 2001, ApJ, 561, 621

Roche C., et al., 2024, arXiv

Rossetti M., et al., 2016, MNRAS, 457, 4515

Schaye J., et al., 2015, MNRAS, 446, 521

Schneider P., 2006, Extragalactic Astronomy and Cosmology. Springer Berlin Heidelberg, Berlin, Heidelberg

Scrucca L., Fraley C., Murphy T. B., Raftery A. E., 2023, Model-Based Clustering,

Classification, and Density Estimation Using mclust in R. CRC Press

Seppi R., et al., 2023, A&A, 671, A57

Silk J., 1977, ApJ, 211, 638

Somerville R. S., Primack J. R., 1999, MNRAS, 310, 1087

Springel V., 2010, MNRAS, 401, 791

Springel V., White S. D. M., Tormen G., Kauffmann G., 2001, MNRAS, 328, 726

Taylor E. N., et al., 2011, MNRAS, 418, 1587

Tempel E., et al., 2014, A&A, 566, A1

Vogelsberger M., Marinacci F., Torrey P., Puchwein E., 2019, Nat. Rev. Phys., 2, 42

Voit G. M., 2005, Rev. Mod. Phys., 77, 207

Von Benda-Beckmann A. M., D'Onghia E., Gottlöber S., Hoeft M., Khalatyan A., Klypin A., Müller V., 2008, MNRAS, 386, 2345

Vulcani B., Poggianti B. M., Finn R. A., Rudnick G., Desai V., Bamford S., 2010, ApJ, 710, L1

Wen Z. L., Han J. L., 2024, ApJS, 272, 39

West M. J., De Propris R., Bremer M. N., Phillipps S., 2017, Nat. Astron, 1, 0157

Zarattini S., et al., 2014, A&A, 565, A116

Zhang B., Cui W., Wang Y., Dave R., De Petris M., 2022, MNRAS, 516, 26

van den Bosch F. C., Weinmann S. M., Yang X., Mo H. J., Li C., Jing Y. P., 2005, MNRAS, 361, 1203